AN ABSTRACT OF THE THESIS OF

Cole B. McCandlish for the degree of Master of Sciences in Atmospheric Sciences presented on April 28, 1994.

Title: A Study of the Relationship Between Ageostrophy and Dynamical Periodicities of the Tropical Pacific Boundary Layer

Abstract approved: Redacted for Privacy

Eight years (1980–87) of twice-daily high-resolution radiosonde data from a tropical mid-Pacific island station are analyzed to generate time series of the planetary boundary layer (PBL) top pressure, an ageostrophic parameter (related to the divergence), and a parameter of mean PBL specific humidity. Sample spectra of these time series are calculated along with a spectra for nighttime outgoing longwave radiation (OLR) data (centered at a gridpoint near the island station) and compared in order to investigate the relationship between the ageostrophy and dynamical phenomena of the tropical Pacific.

Methods of boundary layer top diagnosis are compared. Data derived methods include temperature inversion detection, humidity jump detection, and wind shear detection. The model based diagnosis method uses a Richardson number scheme. Comparisons between data derived methods and model based methods show good agreement. Correlation coefficients for comparisons are all above 0.91.

In each sample spectra, the dominant peak corresponds to the frequency of the annual cycle. With an estimated annual cycle removed from each of the time series the nighttime (12 GMT) sample spectra for PBL top pressure shows a peak at a frequency that corresponds to the 30–60 day Intraseasonal Oscillation (ISO). Removal of an estimated annual cycle was unsuccessful for the daytime (0 GMT) sample spectra for PBL top pressure, PBL mean specific humidity, and the ageostrophic parameter. Sample spectra of the ageostrophic parameter show peaks in the ISO frequency range for both 12 GMT and 0 GMT even before removal of the annual cycle was attempted. The ISO range peaks remained in the 12 GMT ageostrophic parameter spectrum when the annual cycle was successfully removed.

The nighttime OLR spectrum is dominated by the annual cycle peak and its harmonics. The OLR spectrum also shows a significant peak in the ISO range of periods. Removal of an estimated annual cycle intensifies the peak in the ISO range.

The ageostrophic parameter time series is compared to the results of an EOF analysis performed on the same 8 years of radiosonde humidity measurements. The first three EOF modes of specific humidity give sample spectra which are dominated by the annual cycle. With the annual cycle removed the sample spectra of the first and third EOF modes of specific humidity both show significant peaks in the ISO frequency range, while the second EOF mode sample spectrum is dominated by two peaks at frequencies corresponding to periods of approximately 4 and 5 months.

The presence of common frequencies in the ISO range of the power spectra of the ageostrophic parameter (a measure of divergence), the nighttime OLR (a measure of deep convection), the nighttime planetary boundary layer top, and the first EOF mode of specific humidity, lends support to theories that relate the ISO to the interaction of dynamics and moist processes.

A Study of the Relationship Between Ageostrophy and Dynamical Periodicities of the Tropical Pacific Boundary Layer

by

Cole B. McCandlish

A THESIS

submitted to

Oregon State University

in partial fulfillment of
the requirements for
the degree of

Master of Science

Completed April 28, 1994
Commencement June 1995

APPROVED:

Redacted for Privacy

Professor of Atmospheric Sciences in charge of major

Redacted for Privacy

Head of department of Atmospheric Sciences

Redacted for Privacy

Dean of Graduate School

Date thesis is presented April 28, 1994

Typed by Cole McCandlish for Cole B. McCandlish

Acknowledgments

I would like to acknowledge the guidance and extreme patience of my advisor Dr. Gad Levy and his willingness to let me pursue this research at my own pace even though, at times, it must have been much like having ones teeth pulled without novocaine by a blindfolded dentist.

I would also like to thank Dr. Mahrt and Dr. Coakley for allowing the use of their computing facilities in times of crisis. Thank you also to Dr. Esbensen and Dr. Vong for their advice and suggestions throughout this analysis.

Furthermore, I would like to thank my contemporary graduate students for the give and take relationship I have enjoyed with them both academically and in friendship. Special thanks to Jim for sharing his work, and to Andy and Fu-Lung for their continuing friendship (and in one case a roof to live under).

To my family and friends, and to those of my most treasured Kathleen, I provide the following answers: It is finished. , I am finished. , and Please find me a good job.

Finally, I would like to thank the infamous cartoon coyote, who even now is undoubtedly contemplating yet another impact on the canyon floor, for instilling upon me his true genius: the ability to persevere despite the failure of master plans, repeated blows to the head, and faulty consumer goods.

Funding for this research was provided by the National Oceanic and Atmospheric Administration (NOAA) under grant # NA366P0115. Early portions of this research were also supported by a grant from the Caltech Presidents Fund # PF-355.

TABLE OF CONTENTS

List of Figures

List of Tables

A Study of the Relationship Between Ageostrophy and Dynamical Periodicities of the Tropical Pacific Boundary Layer

1. Introduction

In 1971, spectral analysis of nearly ten years of rawinsonde data taken from a tropical station (Canton island, 3° S, 172° W) revealed a previously undiscovered peak in the power spectra of surface pressure, temperature at various levels, and zonal winds associated with a broad range of periods with a maxima between 41 and 53 days (Madden and Julian, 1971). Previous spectral analyses of tropical data were limited by short (less than two years) and sparsely distributed data sets (e.g. Wallace and Chang, 1969). A follow up study in 1972 confirmed the existence of the peak in the 40–50 day range in many tropical stations far away from the original station studied in the first paper and a relative maxima in coherence in the 40–50 day range for stations from Raoul Island (29.2° S, 177.9° W) in the south to Midway (28.2° N, 177.4° W) station in the north (Madden and Julian, 1972). This discovery sparked a new wave of tropical research to determine its characteristics and cause.

The Madden-Julian oscillation, MJO, has a strong relationship with maxima (minima) of convection and wind stress anomalies but so far has no accepted physical explanation. The MJO is not strictly periodic but has a preferred time scale of 30–60 days. Tropical zonal wind anomalies show a phase difference between the upper and lower tropopause. The intraseasonal oscillation (ISO) does not show systematic seasonal variation in either amplitude or periodicity but has

been found to show seasonality in the presence of maximum outgoing longwave radiation (OLR) variability (Knutson and Weikmann, 1987). OLR is commonly used as a measure of deep convection (e.g. Knutson and Weikmann, 1987)

Similarities between the MJO and atmospheric Kelvin waves were presented by Madden and Julian in the 1971 paper, but the Kelvin wave propagates too quickly to be consistent with the observed oscillation. A better first-order model of the ISO can be constructed as a coupled Rossby-Kelvin mode (Gill, 1980).

Since 1972, many other observational studies have shown spectral peaks with periods of 30–60 days in many different tropical data sets. Frictional torque in the tropics was found to have large 40–50 day oscillations with the largest variations in wind stress occurring poleward of 10° latitude (Madden,1988). Atmospheric angular momentum has been shown to have a 40–50 day peak in tropical spectra (e.g. Gutzler and Madden, 1993). Normalized outgoing longwave radiation (OLR) data show 40–50 day oscillations dominating the intraseasonal variability of tropical convection (Lau and Chan, 1985). Oscillations with periods of 40–50 days have been observed in longshore currents and in ocean temperatures (Mysack and Mertz, 1984). The term intraseasonal oscillation (ISO) is used to encompass all phenomena that have significant spectral peaks in the range of periods between 30 and 60 days.

General circulation model (GCM) simulations suggest that the ISO is most likely an interaction between atmospheric dynamics and condensational heating (e.g. Goswami and Shukla, 1984). The ISO can occur in GCM's that do not have

continents or seasonal variations, but never occurs in models that do not have a latent heat release mechanism (Hartmann and Gross, 1988).

Cho et al., (1994) used a model to conclude that the ISO is caused by latent heat release in organized cloud clusters and not directly from the presence of cumulus convection. If the convective heating field is prescribed and held constant with time, no 40–50 day oscillations occur in a model (Goswami and Shukla, 1984). Thus, according to model simulations, the ISO requires a time varying convective heating field, and a mechanism of latent heat release.

Other model results suggest that intraseasonal oscillations exist in the atmosphere without a dynamically interactive ocean (Lau and Peng, 1987) or cloud radiation feedbacks (Hayashi and Golder, 1986), but that strong air-sea interaction between outgoing longwave radiation (OLR) anomalies and the 40–50 day oscillation may amplify the OLR anomaly during El Nino/Southern Oscillation (ENSO) (Lau and Chan, 1985). Thus, there seems to be a purely atmospheric 40–50 day oscillation that can be amplified with strong air-sea interaction.

The ISO was found to have no systematic seasonal variations in the amplitude or frequency (Anderson, et al., 1984). The magnitude of the 40–50 day spectral peak in the zonal wind power spectrum was found to be higher in nothern hemisphere (NH) winter and lower in the NH summer (Madden, 1986). A seasonal study of ISO using equatorial radiosonde data suggests that the ISO period decreases in late NH spring and early NH summer to a value less than 40 days and that during late NH winter and late NH summer the period is closer to 50 days (Hartmann et al., 1992).

Lau and Chang, (1992) reported model results with a 20–30 day period in the velocity potential field and suggested that this might represent possible communication between the tropics and subtropics. A 24–28 day period was presented in Ghil and Mo, (1991) which, the model showed, was predominant in the drier E. Pacific region. Models have a tendency to allow anomalies to propagate too rapidly (e.g. Hayashi and Golder, 1986 and Lau and Peng, 1987) and these shorter periods could be the result of the models speeding up the ISO phenomena. Hartmann et al., (1992) used equatorial radiosonde data to suggest a relationship with the preferred recurrence period for typhoons (15–25 days) and that the 20–25 day oscillation may modulate the occurrences of typhoons.

This analysis will examine the relationship between boundary layer integrated properties and the various ISO phenomena in terms of boundary layer depth, boundary layer moisture, and boundary layer divergence. The analysis of integrated boundary layer quantities and the more Northern location of the data site in the tropics, are both unusual for ISO studies, and will hopefully yield new information about the ISO phenomena.

2. Background

2.1 The Ageostrophic Parameter

The ageostrophic parameter (Levy and Bretherton, 1987) is a measure of the ageostrophy of the flow. Ageostrophy is the deviation from geostrophy. In the boundary layer, wind speed is directly influenced by friction with the Earth's surface. The primary force balance (away from the equator) for a steady-state, horizontally homogeneous planetary boundary layer, PBL, is made up of three components: pressure-gradient force, the Coriolis force, and a friction term.

Equations 1a and 1b represent the x and y component respectively of the simplified equation of motion within the PBL. The first term in each equation is the pressure-gradient term where p is pressure, ρ is the density of air. The second term in the equations is the Coriolis term where f is the Coriolis parameter and u and v represent the x and y component of velocity. The third term in the equations represents the influence of friction.

$$0 = -\frac{1}{\rho}\frac{\partial \overline{p}}{\partial x} + f\overline{v} - \frac{\partial \overline{u'w'}}{\partial z} \tag{1a}$$

$$0 = -\frac{1}{\rho}\frac{\partial \overline{p}}{\partial y} - f\overline{u} - \frac{\partial \overline{v'w'}}{\partial z} \tag{1b}$$

The frictionally induced cross isobar flow at the lowest level of the atmosphere implies surface divergence of air. If air is assumed to be an incompressible fluid, the build up of mass via convergence must ascend by continuity.

$$\frac{\partial u}{\partial x} + \frac{\partial v}{\partial y} = -\frac{\partial w}{\partial z} \tag{2}$$

Thus, negative horizontal divergence that corresponds to cross isobar flow into a surface low implies positive (upward) vertical motion. This vertical motion further implies a secondary circulation throughout the PBL as shown in figure one.

Above the PBL the primary force balance for the wind is a near balance between the pressure-gradient force and the Coriolis force, which results in flow parallel to isobars (geostrophic flow).

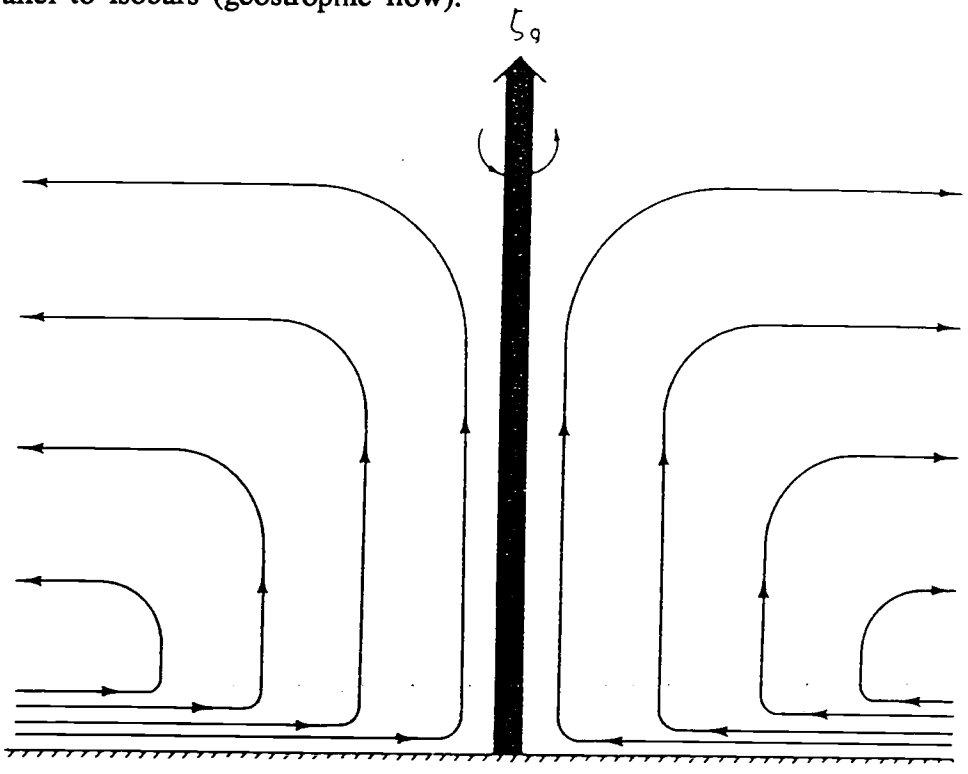

Figure 1 Plot of Frictionally Induced Secondary Circulation (Holton, 1992)

In rotational flows, vorticity is often used to describe motion because of its relationship to the local angular velocity of the fluid. The vertical component of relative vorticity is defined as

$$\zeta \equiv \frac{\partial v}{\partial x} - \frac{\partial u}{\partial y} \tag{3}$$

and represents the effect of the rotation of the fluid on the microscopic scale. The vorticity is the average circulation per unit area. Thus, an increase in area due to horizontal divergence implies a decrease in vorticity to conserve the circulation. Scale analysis shows that the divergence term is the largest scale term of the equation for the rate of change of vorticity (Holton, 1992). Divergence itself is a very difficult quantity to measure accurately (Holton, 1992), but by using the relationship between vorticity and divergence a surrogate parameter can be created that is more easily obtained from conventional data.

The ageostrophic parameter, C, is defined in terms of easily measured quantities (readily available from rawinsonde data), by the following relation:

$$C \equiv \frac{\zeta_g}{\zeta_t} = \frac{\zeta_g}{\zeta_g + \zeta_a} = \frac{G}{S\cos\alpha} \tag{4}$$

The ratio ζ_g/ζ_t relates the geostrophic relative vorticity to the total (geostrophic+ageostophic) relative vorticity. In the case of purely geostrophic flow (the absence of friction) this ratio is exactly one. In the above equation, G is the geostrophic wind speed, S is the surface wind speed, and α is the turning angle (the angular difference between the surface wind direction and the geostrophic wind direction). The assumptions involved in deriving equation 4 are detailed in Levy and Bretherton, (1987) and are expected to hold for this study.

The deviation of this ratio from one, indicates the influence of surface friction and characterizes the extent of ageostrophic (divergent) flow in the boundary layer. The ageostrophic flow is related to a secondary circulation induced by boundary layer friction. It is this relationship between the ageostrophic flow, the surface

divergence, and the vertical motion that may allow the ageostrophic parameter to be useful in characterizing integrated dynamical properties of the PBL.

2.2 Climatology of the Tropical North Pacific

During Northern Hemisphere winter the Hadley circulation is strong and the easterly trade winds dominate the circulation. Figure 2 shows a plot of mean sea level pressure for the North Pacific for January. The pattern is dominated by the strong Low in the North Pacific and a relatively weak subtropical High off the SW coast of the US. The mean sea level pressure pattern for July is shown in figure 3. This plot shows a subtropical High dominating the entire Northern Pacific.

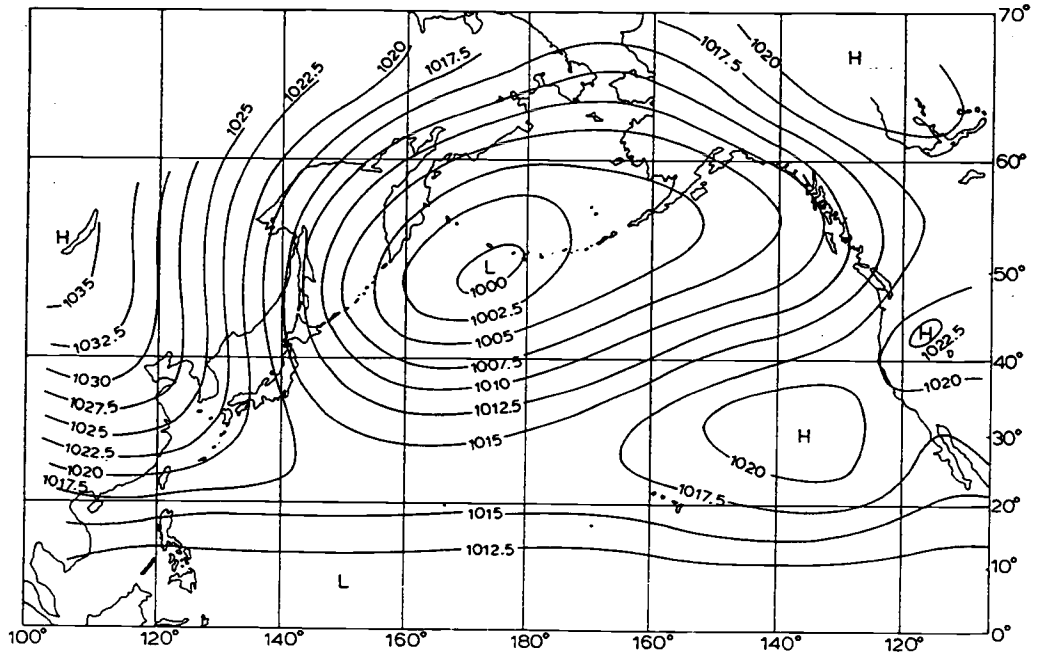

Figure 2 Mean Sea Level Pressure Pattern of the North Pacific, January (Terada and Hanzawa, 1984)

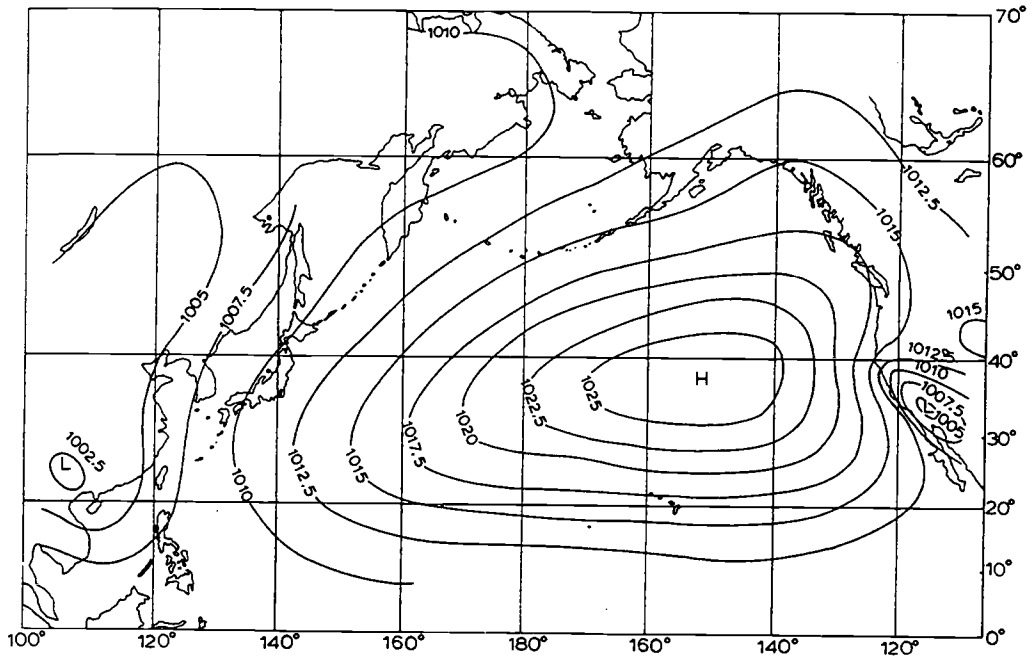

Figure 3 Mean Sea Level Pressure Pattern of the North Pacific, July (Terada and Hanzawa, 1984)

The subtropical high causes anti-cyclonic motion, and large scale subsidence keeps moisture trapped below the trade inversion. The anti-cyclonic flow on the eastern flank of the subtropical high produces westward and equatorward movement of air. The air then moves from the subtropical region of large subsidence to the tropical region of increasing convergence. The moisture that was trapped by the trade inversion gradually penetrates the inversion as convergence is enhanced with motion towards the equatorial convergence zone. The result of the convergence is increased cloudiness and precipitation in the tropics (Hastenrath, 1990).

The position of the equatorial convergence zone (called the intertropical convergence zone, ITCZ) is seasonally dependent. During Northern Hemisphere

(NH) winter the northern edge of the ITCZ is confined near the equator. In NH summer the ITCZ can extend to 10° N over the oceans. Many tropical stations do not receive significant rainfall until the ITCZ is near their latitude since the overwhelming large scale feature otherwise in the tropics is subsidence. Without the enhanced convection that the ITCZ brings, moisture and air are trapped under trade inversions.

The average wind direction is predominantly easterly throughout the year. During the months when the ITCZ has little influence, the average wind direction is ENE as shown in figure 4. In June through September, when the ITCZ is dominant, the average wind direction is easterly as shown in figure 5 (Terada and Hanzawa, 1984).

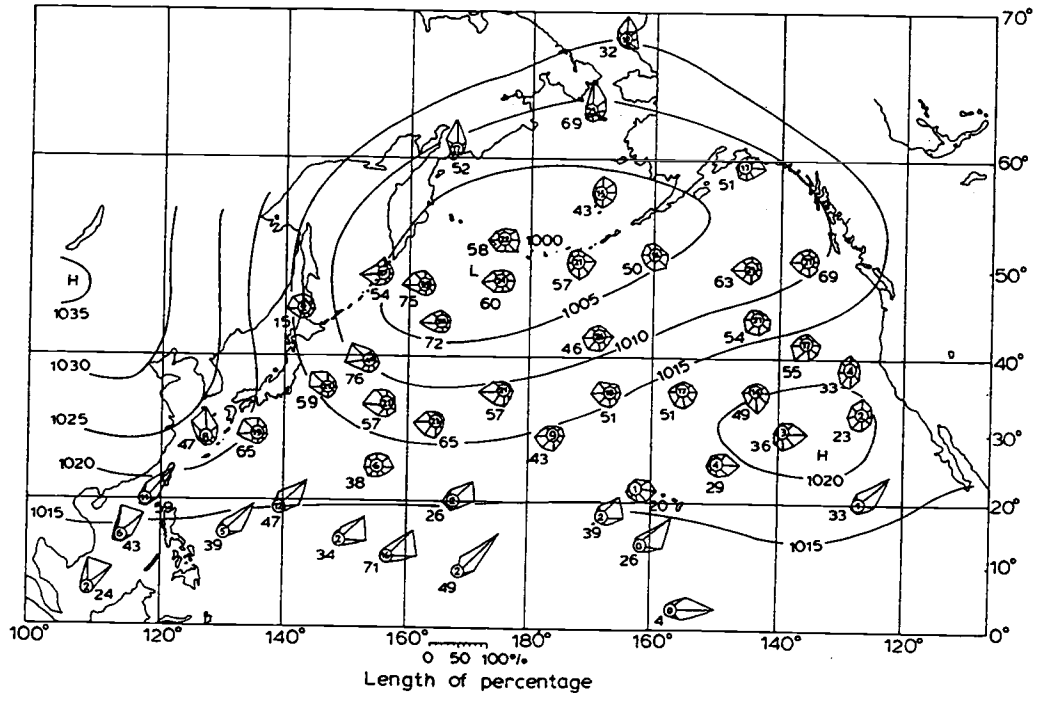

Figure 4 Wind Roses for the North Pacific, January (Terada and Hanzawa, 1984)

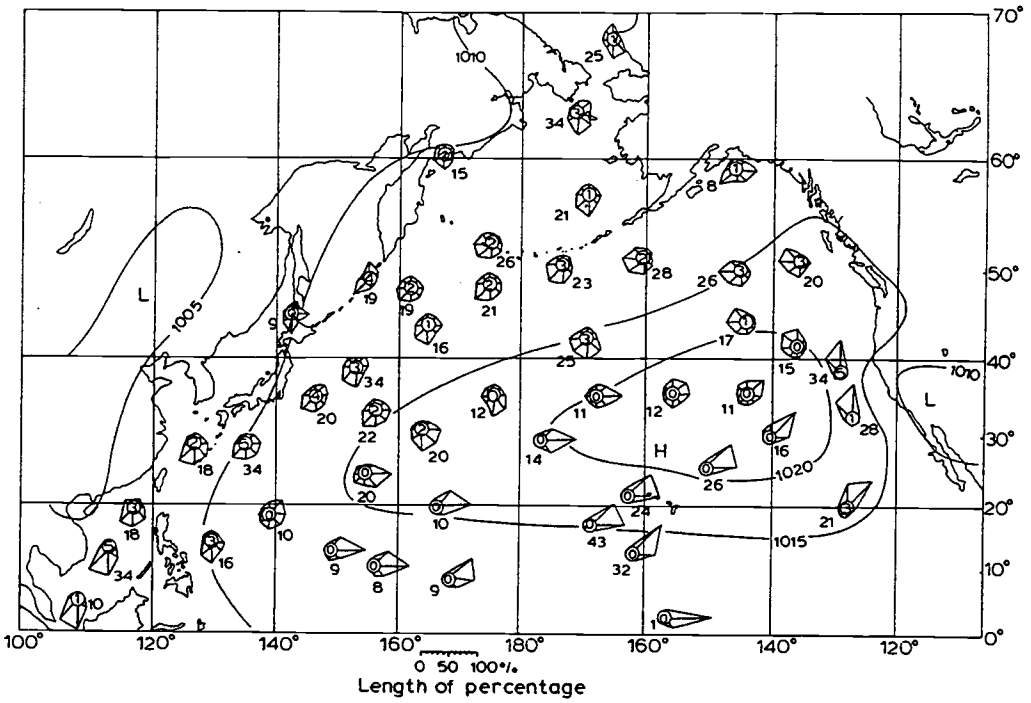

Figure 5 Wind Roses for the North Pacific, July (Terada and Hanzawa, 1984)

2.2.a Intraseasonal Oscillation (ISO)

The term intraseasonal oscillation (ISO) will refer to all phenomena known to exhibit a 30–60 day spectral peak in tropical data. ISO includes the Madden-Julian Oscillation (MJO) found in tropical surface pressure and wind spectra (Madden and Julian, 1971 and Madden and Julian 1972), atmospheric angular momentum (AAM) (Madden, 1986), and tropical OLR data (e.g. Knutson and Weikmann, 1987) which have been discussed previously in the introduction.

3. Data and Methods

Rawinsonde data from a station on Wake island in the mid-Pacific (corresponding to the data used by Liu et al., 1991) were obtained from the Jet Propulsion Laboratory (JPL). The data are twice daily (0 /12 GMT) high-resolution vertical soundings of pressure, temperature, specific humidity, wind speed and wind direction. Local time at 0 GMT is 12 noon of the same day thus Wake local time is twelve hours ahead of GMT.

Wake island is located in the Northeastern Tropical Pacific at 19.17 °N latitude and 166.6 °E longitude. The location of Wake island is labelled on the map shown in figure 6. Wake island is within the area tested for coherence with the ISO signal discovered at Canton island (Madden and Julian, 1972). Wake island was chosen for its tropical location, and its more Northerly position in the tropics that allows for a better assumption of Coriolis/pressure-gradient force balance than a more equatorial station. As one approaches the equator the Coriolis term in the first order wind balance becomes smaller and no longer balances the pressure-gradient term. At Wake island the assumption of Coriolis/pressure-gradient balance is still viable.

There are a total of 5735 soundings for the period from 1980–87. The data are quite complete in terms of the requirements of a boundary layer study, every sounding in the set is complete to at least the 100 mb level. The only notable instance of missing data occurs during 1983, where one month (April) of wind speed and direction data are missing. These 60 records cannot be used to calculate the ageostrophic parameter, but have been included in the PBL top diagnosis by

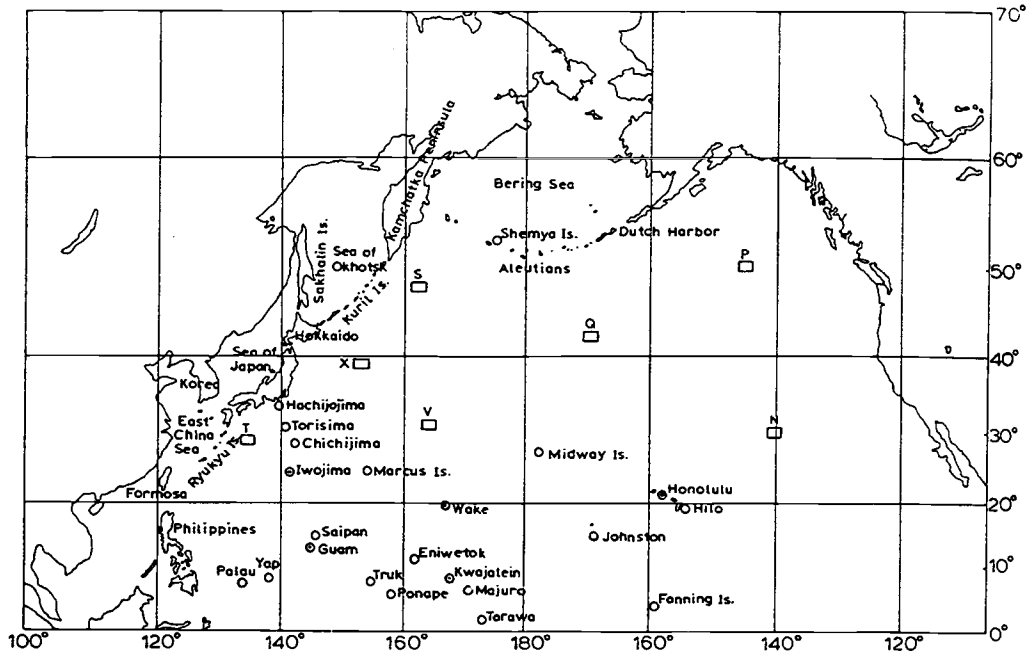

Figure 6 Map of North Pacific Ocean (Terada and Hanzawa, 1984)

using the two methods that do not require wind data. The PBL top time series has 5735 values and the ageostrophic parameter time series has only 5675 values. Comparisons between time series were performed with the common 5675 values available to each time series.

3.1 Determination of the PBL Top

Beginning with twice-daily rawinsonde data for Wake island for the year 1980, a time series of the ageostrophic parameter was constructed. A computer program was created to calculate this time series. To begin construction of the ageostrophic parameter time series it was necessary to first determine the top of the planetary boundary layer (PBL) for each sounding.

Diagnosing the top of the planetary boundary layer is crucial to the calculation of the ageostrophic parameter. The geostrophic wind speed contained within the parameter can be obtained by assuming that the flow is near geostrophic above the PBL and that the flow at the level above the PBL top is an adequate representation of the geostrophic flow. Thus after determining the PBL top, one can simply read off the corresponding geostrophic values from the sounding data.

There are many assumptions that go into any attempt to identify the PBL top, including the definition of the PBL top itself. A general definition of the PBL is: the lowest portion of the atmosphere in which the effects of surface induced friction are important on some specified time scale (Stull, 1988). Measuring the effects of friction on the Earth's surface would be quite difficult and require some type of drag plate experiment (as described in Batchelor's Fluid Dynamics for example).

Other definitions allow the PBL to extend to the tropopause (possibly because the tropopause is much easier to identify from real sounding data). Still another definition refers to the mixing length of large eddies and incorporates the presence of turbulence as a criteria. For the purposes of this paper, the PBL will be characterized as follows: within the PBL the flow is turbulent, the PBL contains most of the water vapor in the atmosphere, the wind speed is subgeostrophic in the PBL, and the PBL top can be determined easily in the case of a temperature inversion (the bottom of the inversion marks the top of the PBL). Four different methods are applied to the data in order to define the PBL based on the above characteristics.

Determination of the PBL top is most difficult for highly convective cases. These are cases that have very unstable temperature profiles and usually no discernible temperature inversion below the tropopause level. There is some debate as to whether or not a PBL top can be defined in cases of strong convection. For cases of strong convection, the PBL top is often taken to be cloud base height which can be much lower than PBL top heights associated with strongly stable conditions (Stull, 1988).

In order to maximize the number of data records used in the analysis four methods were compared to determine the PBL top and a combination of these methods was implemented.

3.1.a Temperature inversion detection

Temperature profiles were analyzed to detect an inversion (a layer of increasing temperature with increasing height) that would indicate the top of the PBL. In some cases the first detectable inversion was at a height below 150 meters which, although possible, is generally considered too low to represent the top of the tropical PBL. In these cases, the next inversion above 1000 mb was selected to represent the PBL top. Out of the 5735 soundings only 177 yielded detectable inversions below 1000 mb. Of these 177, all but 34 were properly diagnosed by other methods. The arbitrary 1000 mb cut off affects less than 0.6% of the data used in this study.

A temperature inversion indicates a stable layer of the atmosphere that is very resistant to vertical motions. Thus, any eddy transport through the stable layer

will be suppressed, and the air will be trapped in the layer below. This lower layer is then well mixed by the trapped eddies and forms the boundary layer. By using the temperature data exclusively, one is ignoring the effect of water vapor on the density (and hence buoyancy) of air.

Figure 7 shows an example of the temperature inversion detection method applied to real data. The vertical sounding of temperature shows a well defined inversion between 800 mb and 850 mb. The dashed line represents the diagnosed pressure level of the boundary layer top as determined by the inversion detection algorithm; in this case the PBL top is 824 mb.

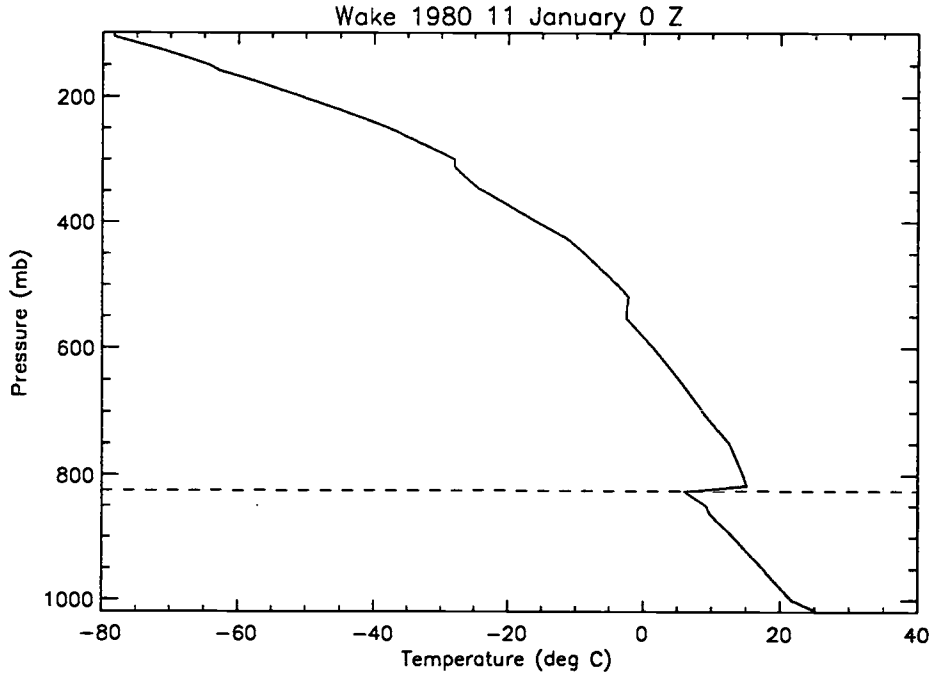

Figure 7 Sample Plot of Temperature Inversion Method.

3.1.b Humidity jump detection

A second method to analyze rawinsonde data to diagnose the PBL top is to examine the vertical profile of specific humidity (q). One can assume that most of the water vapor will be in the boundary layer and that there will be a rapid decrease in q values as one moves away from the sources of humidity and into the geostrophic flow. This method is not always accurate as it tends to give only a zone of decreasing q layers rather than a specific pressure level as in the temperature inversion method. Thus, by detecting this zone of rapid humidity drop one can make an estimate as to the PBL top. In the cases where the zone was several levels deep the lowest level was chosen as the PBL top.

Figure 8 shows an example of the humidity jump detection method as applied to real data. The specific humidity vertical profile clearly shows a region of rapid decrease in q near 850 mb. The dashed line represents the diagnosed boundary layer top pressure level as determined by the algorithm as 850 mb. In this case the diagnosed value could vary between 850 mb and 846 mb, but the difference between these values is not significant to the determination of the geostrophic winds, since radiosonde data is not taken at regular intervals of pressure values.

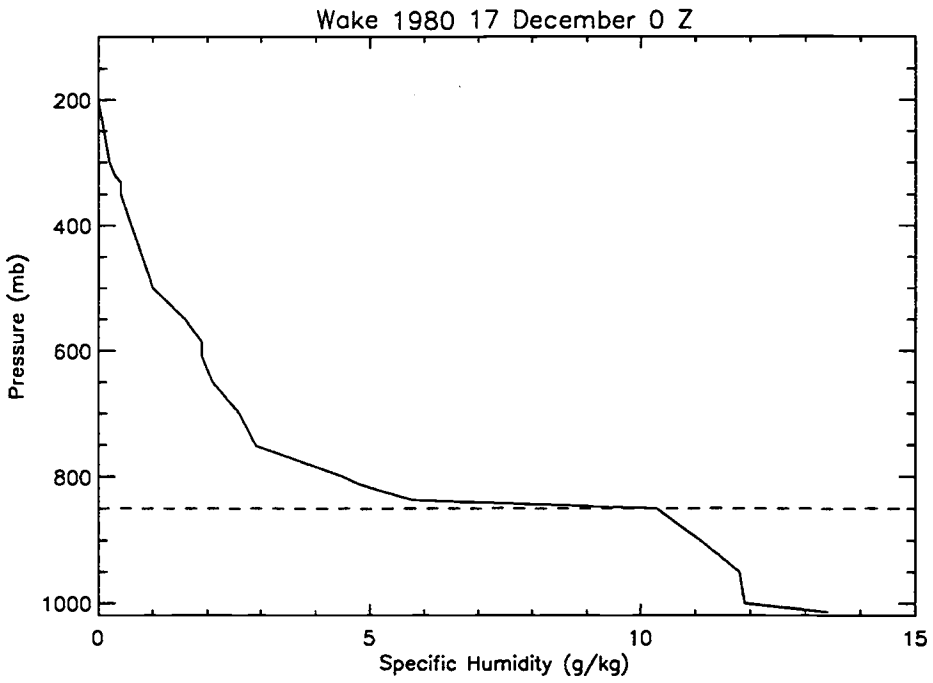

Figure 8 Sample Plot of Humidity Jump Detection Method.

3.1.c Wind speed difference detection

Still another method for diagnosing the PBL top from rawinsonde data is to look at the vertical profile of wind speed. The PBL is the region of the atmosphere that is under the influence of surface friction. Friction acts to reduce wind speeds in the PBL. The geostrophic flow is not influenced by friction, but rather by baroclinicity, thus the measured wind speeds in the idealized case should be greater in the geostrophic flow than in the PBL flow. By looking for a sudden increase in wind speed over a narrow layer thickness (large vertical shear), one can estimate the PBL top. As in the humidity case this method tends to yield a zone of transition rather than a specific pressure level.

These three methods make up a diagnosis scheme that is derived from looking at raw data. Only zero wind speed values have been changed at this stage. The zero surface wind speeds would cause the ageostrophic parameter to become infinite for that sounding, and were replaced by the second level wind speed of the sounding.

3.1.d Model based diagnosis

The fourth method of PBL top diagnosis exploits an assumption about turbulence in the PBL. If one assumes that turbulence only occurs in the PBL, then one can use a turbulence detection method to determine at what level turbulence stops, and therefore the level of the PBL top. One such method is based on the calculation of the bulk Richardson number for each sounding level.

The Richardson number is the ratio of the production of turbulent kinetic energy (TKE) due to buoyancy (stratification) effects to the production of TKE due to shear. The bulk Richardson number is defined as

$$R_B = \frac{g\Delta\overline{\theta_v}\Delta z}{\overline{\theta_v}\left[\left(\Delta\overline{U}\right)^2 + \left(\Delta\overline{V}\right)^2\right]} \tag{5}$$

where g is the acceleration due to gravity, $\Delta\theta_v$ is the difference in virtual potential temperature across the layer, Δz is the thickness of the layer, and$\Delta\overline{U}$ and $\Delta\overline{V}$ are the differences in horizontal wind speeds between the top and bottom of the layer and defined as

$$\overline{U} = \overline{U}(z_{top}) - \overline{U}(z_{bottom}) \tag{6}$$

$$\overline{V} = \overline{V}(z_{top}) - \overline{V}(z_{bottom})$$

A theoretical Richardson number of 0.20–0.25 (the so-called critical value) indicates when a non-turbulent (or laminar) flow becomes turbulent. The bulk Richardson number critical value will be slightly higher due to the approximation of the gradients by finite differences. The finite differences depend on the thickness of the layer and thus only approach the theoretical critical value of the Richardson number for thin layers. At a positive value larger than one, the turbulent flow becomes laminar (Stull, 1988).

Since a radiosonde balloon rises from the turbulent PBL to the non-turbulent geostrophic flow, we are interested in determining the level at which the turbulent flow becomes laminar and thus where the Richardson number is just greater than 1.0. By creating a vertical profile of bulk Richardson numbers one can see in the PBL the large negative values of the Richardson number indicating turbulence, and then a region of rapid change to positive values larger that one. By taking the first level with a value of the Richardson number greater than or equal to 1.0, one can estimate the PBL top.

Figure 9 shows a plot of the vertical profile of calculated Richardson number values from an algorithm based on an Oregon State University One Dimensional Planetary Boundary Layer (OSU–1DPBL) model subroutine (Ek and Mahrt, 1991). The surface value is zero due to the lack of surface data which is necessary for the difference calculations. The vertical profile has negative values until it makes a rapid change to positive values around 850 mb. The dotted line represents the boundary layer top pressure level as diagnosed by the algorithm, in this case

840 mb. The profile then returns to constant zero value because the algorithm stops calculating Richardson numbers when it finds a value larger than one.

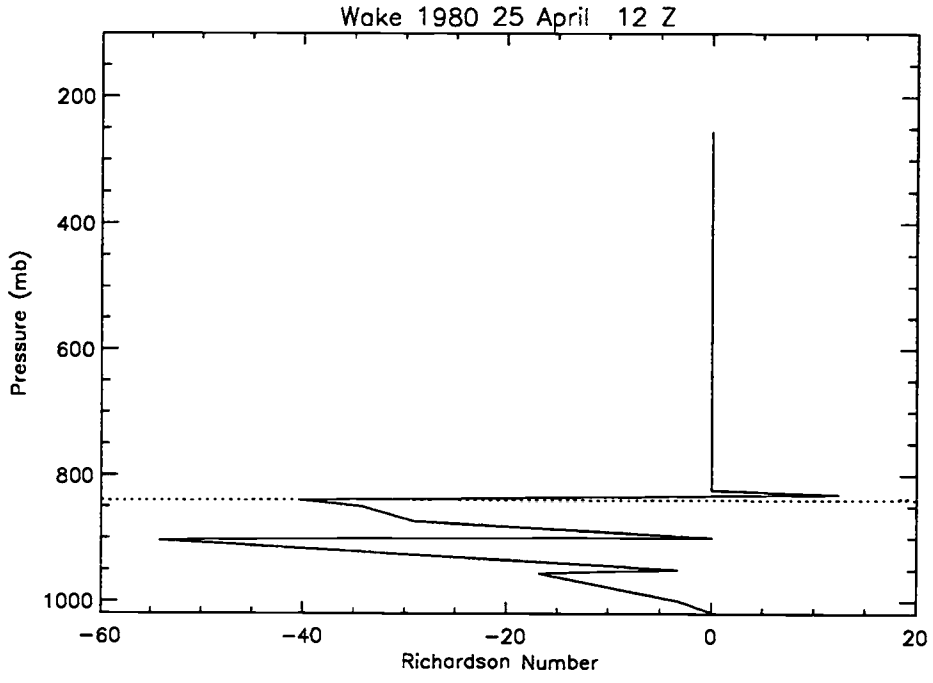

Figure 9 Plot of Richardson Number Transition from PBL to Geostrophic Flow.

TBL is the value of the PBL top pressure that is chosen by comparing the values of the four methods. When two or more of the methods result in the same sounding level for the PBL top pressure, that value of pressure becomes the consensus "top of the boundary layer" pressure, or TBL. It is the time series of TBL that gives the boundary layer height from which the geostrophic wind speed is defined.

From the time series of TBL values, the corresponding wind data were used as estimates for the geostrophic flow. It is assumed that the number of cases of strong baroclinicity (shear of the geostrophic wind) is small in this analysis

and that the wind data values corresponding to the values of TBL do represent the geostrophic flow adequately. Since the baroclinicity is directly related to the horizontal gradient of temperature, and the horizontal gradient of temperature in the tropics is in general small, the number of cases with high baroclinicity should also be small.

In cases of strong baroclinicity in the PBL the estimate of the ageostrophic parameter obtained by using two levels of wind data will be contaminated by the presence of a geostrophic shear component and thus would no longer be valid. In these cases the ageostrophic parameter should be calculated using a value for the geostrophic wind obtained from the horizontal pressure gradient instead of the two level method used in this paper, and a correction term may be required to make equation 4 more accurate.

A time series of the ageostrophic parameter was constructed. Similarly, using the TBL time series, corresponding specific humidity data were used to construct a time series of an integrated PBL moisture parameter.

The boundary layer moisture parameter, Qdif, is simply the difference between first sounding level specific humidity, q_s, and boundary layer top specific humidity, q_b,

$$Qdif \equiv q_s - q_b \tag{7}$$

Qdif is analogous to mean boundary layer specific humidity flux and is expected to exhibit characteristics that represent integrated boundary layer moisture flux.

3.2 EOF Analysis of Specific Humidity Vertical Profiles

An empirical orthogonal function (EOF) analysis was performed by Liu et al., (1991) on nine years of radiosonde humidity profile data. The analysis was repeated for different averaging time scales ranging from one to thirty days.

An EOF analysis is an attempt to break down the data in terms of a set of N orthonormal functions, $F_i(p)$, along with uncorrelated time amplitudes, $C_i(t)$. For the vertical profile of specific humidity which depends on pressure as a vertical coordinate and time, q(p,t), the form of the decomposition is:

$$q'(p,t) = \sum_{i=1}^{N} C_i(t) F_i(p) \tag{8}$$

where the prime indicates the deviation from the temporal mean (Liu et al., 1991).

The principle component, or EOF mode, is then described by the ith coefficient

$$C_i(t) = \sum_{i=1}^{N} q'(p,t) F_i(p) \tag{9}$$

which represents the variance assigned to the ith mode (Liu et al., 1991).

The fraction of the total variance explained by any component, i, is

$$a_i = \frac{\alpha_i}{\sum_{j=1}^{N} \alpha_j} \tag{10}$$

where α is the eigenvalue of the covariance matrix of q. The percentage of the total variance explained by any component, i, is

$$b_i(p) = \frac{\alpha_i F_i^2(p)}{\sum_{j=1}^{N} \alpha_j F_j^2(p)} \tag{11}$$

(Liu et al., 1991).

Liu et al., (1991) determined that for an averaging period greater than two weeks, approximately 90% of the variance in vertical water vapor profiles could be explained by the first mode. For a daily averaging period they determined that three independent modes were required to explain 80–90% of the variance.

EOF analyses have been used in analysis to estimate the number of processes that may be responsible for most of the variability (e.g. Wallace, 1972). Thus it is the first three modes of Liu's analyses, and the processes they represent, that are of interest when looking at time scales less than two weeks.

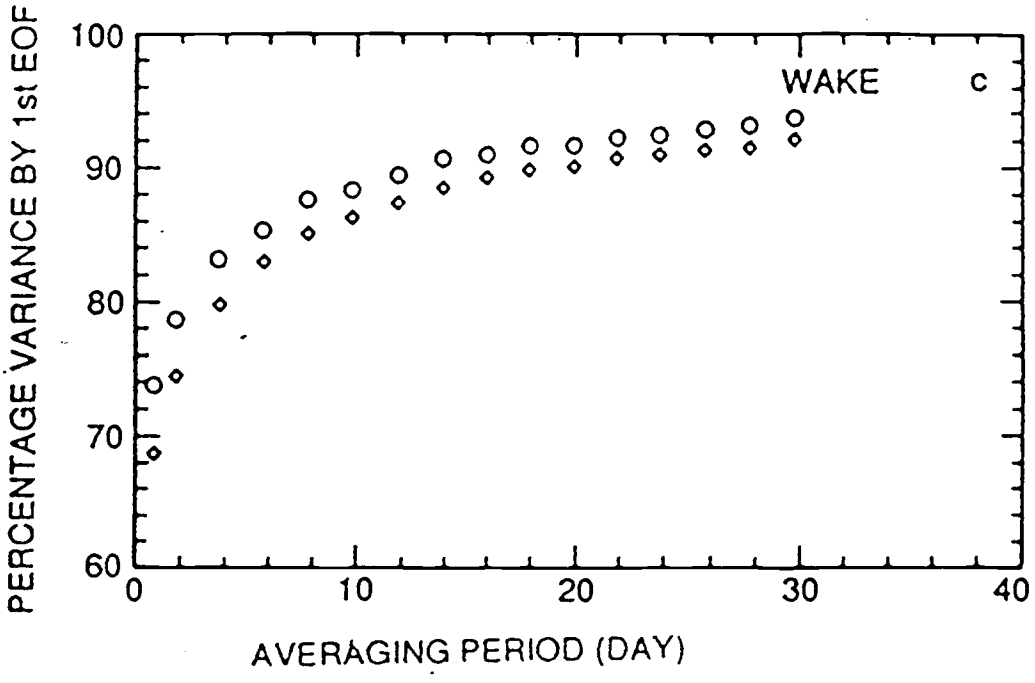

Figure 10 Plot of First Mode Variance Percentage vs Averaging Period (Liu et al, 1991). Refer to text for explanation of symbols.

Figure 10 shows the effect of increasing averaging period on the percentage of total variance explained by the first EOF mode. The two sets of data reflect experiments performed on soundings cut off at the 850 mb level (the lower set of data points) and the same analysis performed on the same soundings that were continued to the 500 mb level. Liu et al., (1991) chose a fixed boundary layer height of 850 mb for their analysis.

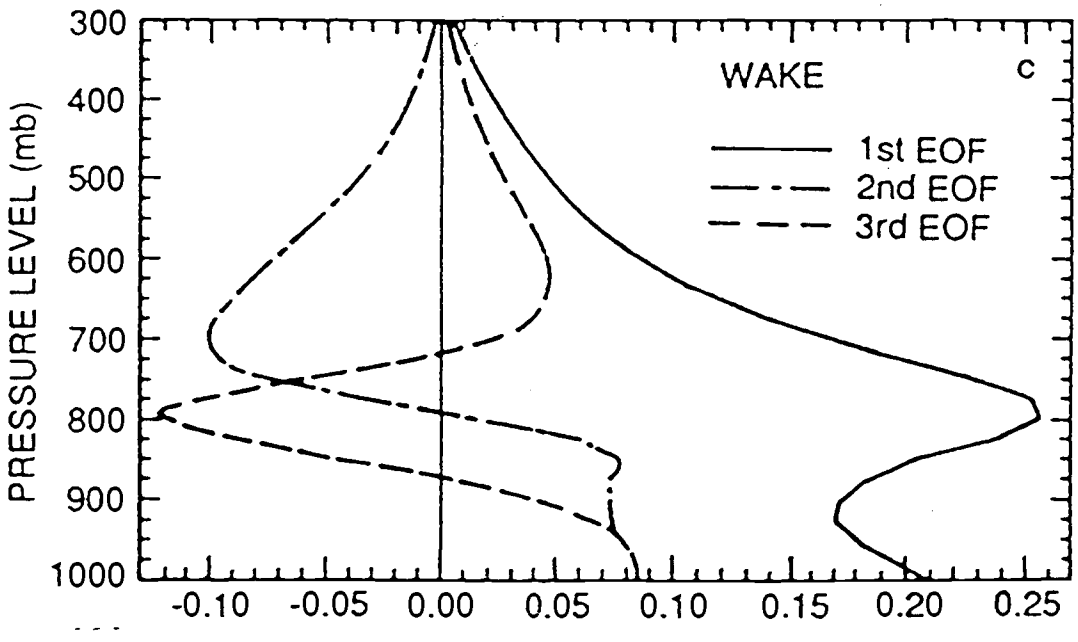

Figure 11 Plot of EOF of Specific Humidity Leading Modes (Liu et al., 1991)

The vertical profiles of the three EOF modes of specific humidity, shown in figure 11, suggest a relationship to the planetary boundary layer. Each profile has an inflection point near 800 mb which is similar to average boundary layer top

pressure. The inflection points near this value seem to indicate a difference in behavior of the modes between the boundary layer and the free atmosphere above.

The first and dominant mode, shown in figure 12, has been determined by Liu et al., (1991) to be highly correlated to the monthly mean of integrated water vapor of the overlying atmospheric column. The eight peaks in the time series show the strong annual cycle. Figure 13 is a plot of the same data shown in figure 12 but has been filtered by a routine based on the Haar transform (Mahrt and Howell, 1994) for presentation purposes. Both figures have been presented here for comparison, but future figures will show filtered data for clearer presentation.

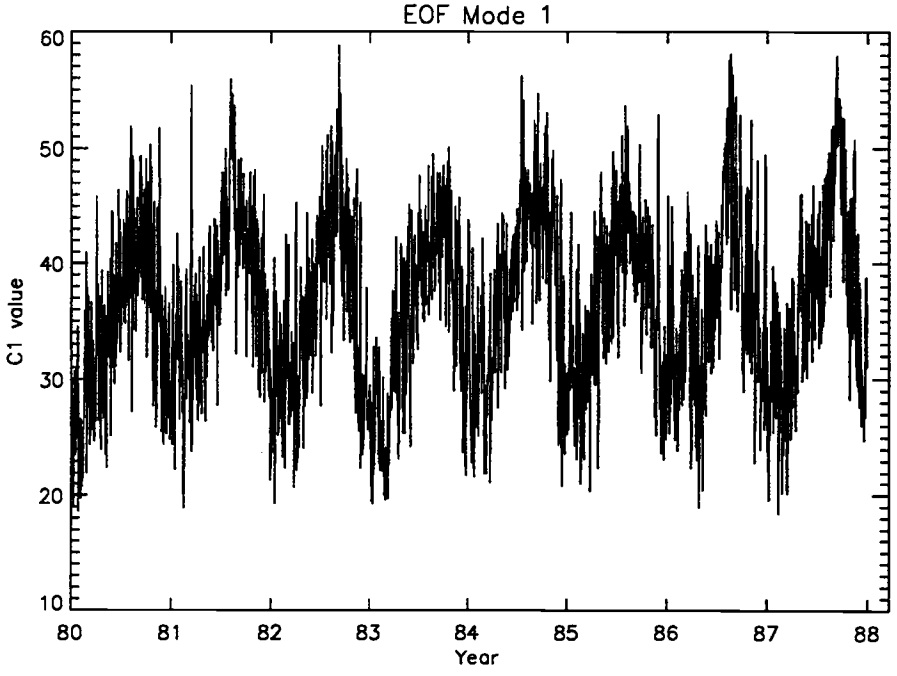

Figure 12 Plot of First EOF Mode Time Series, C1

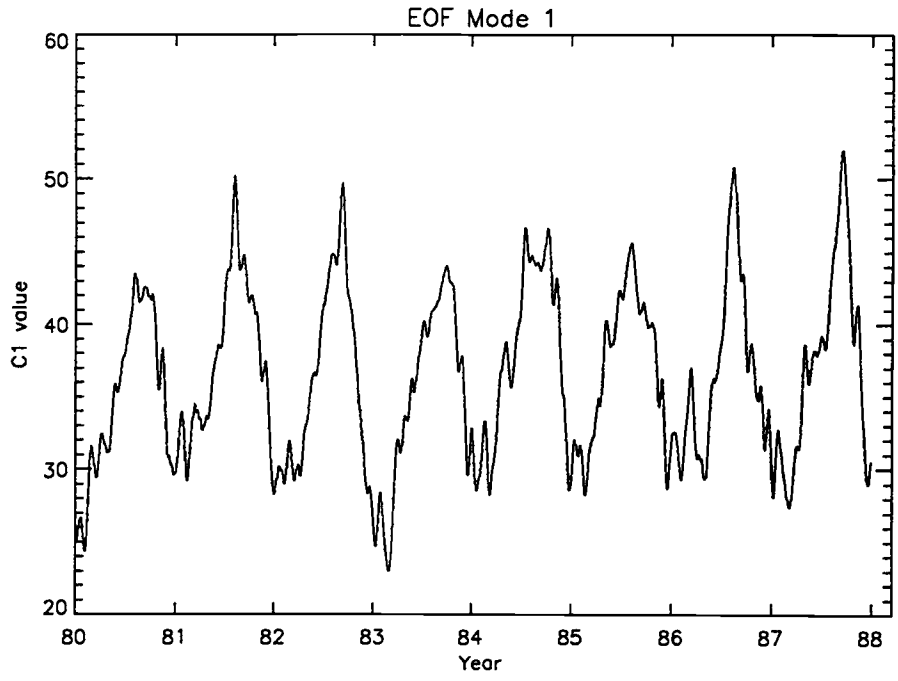

Figure 13 Plot of Filtered First EOF Mode Time Series, C1

Liu et al., (1991) attempted to relate two parameters (neither of which were operationally derivable from satellite data) to the second mode (shown in figure 14) with very little success. Neither the second mode or third mode (shown in figure 15) have been related to a specific physical or dynamical process.

An EOF analysis does not attach physical significance to the various modes, it merely provides the percentage of variance explained by the mode. Thus, a mode may represent the combination and interaction of many physical processes and may not be correlated to any single physical phenomenon.

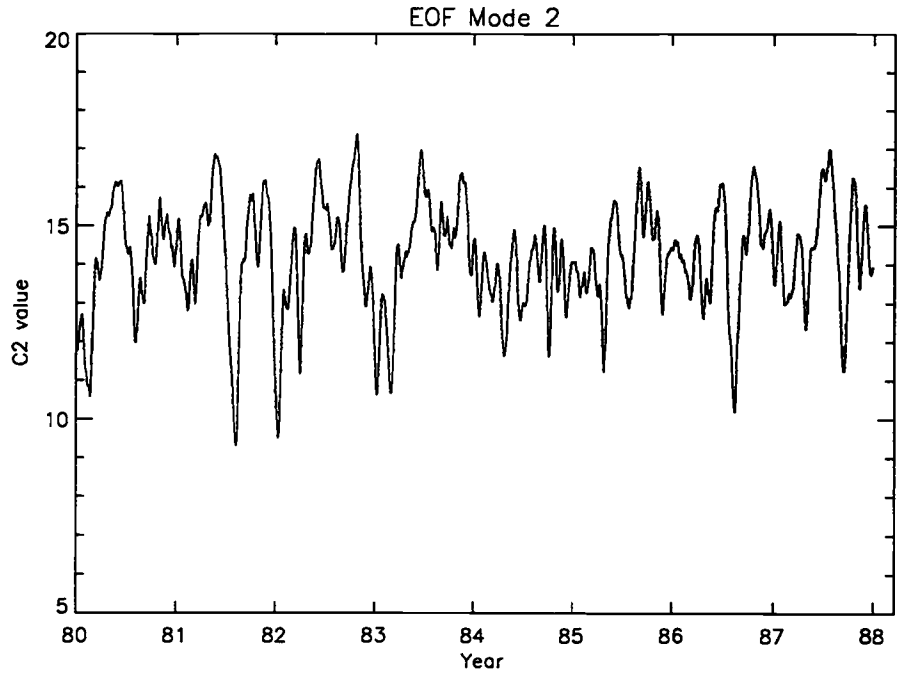

Figure 14 Plot of Filtered Second EOF Mode Time Series, C2

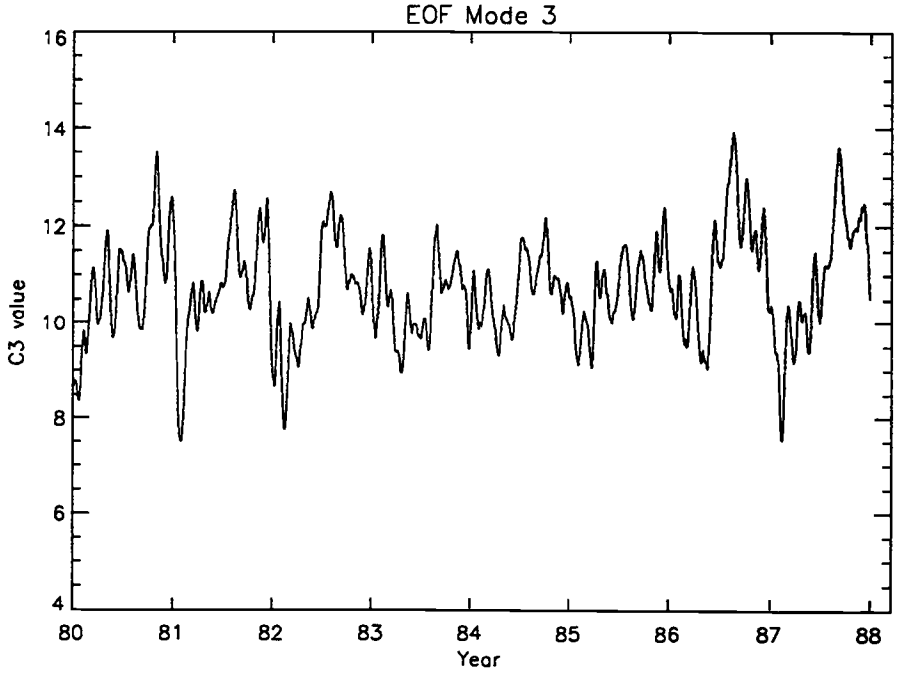

Figure 15 Plot of Filtered Third EOF Mode Time Series, C3

3.3 Determination of Stratification

The stratification for each sounding was determined by calculating the value of the bulk Richardson number at the lowest sounding levels. The finite differences that approximate the partial derivatives were calculated between the first and second sounding levels. The bulk Richardson number retains the same sign as the static stability parameter, z/l, from the Monin-Obukhov similarity theory. A negative value of the bulk Richardson number (and therefore z/l) indicates an statically unstable sounding, and a positive value corresponds to a statically stable sounding (Stull, 1988).

3.4 Reduction of Variance

A frequency distribution histogram of boundary layer top values, figure 16, was created for each method of PBL top determination. Since each of the histograms are consistent with the shape of a normal distribution, it is assumed that a normal distribution will appropriately model the true population of boundary layer top values.

Distributions of PBL top values were assumed to be approximately normal and any values outside of three standard errors from the mean were considered possible outliers. In a normal distribution 95% of the values are within two standard deviations of the mean. Thus there is less than a 5% chance of throwing away a real member of the population by removing values outside of a three standard deviation interval about the mean.

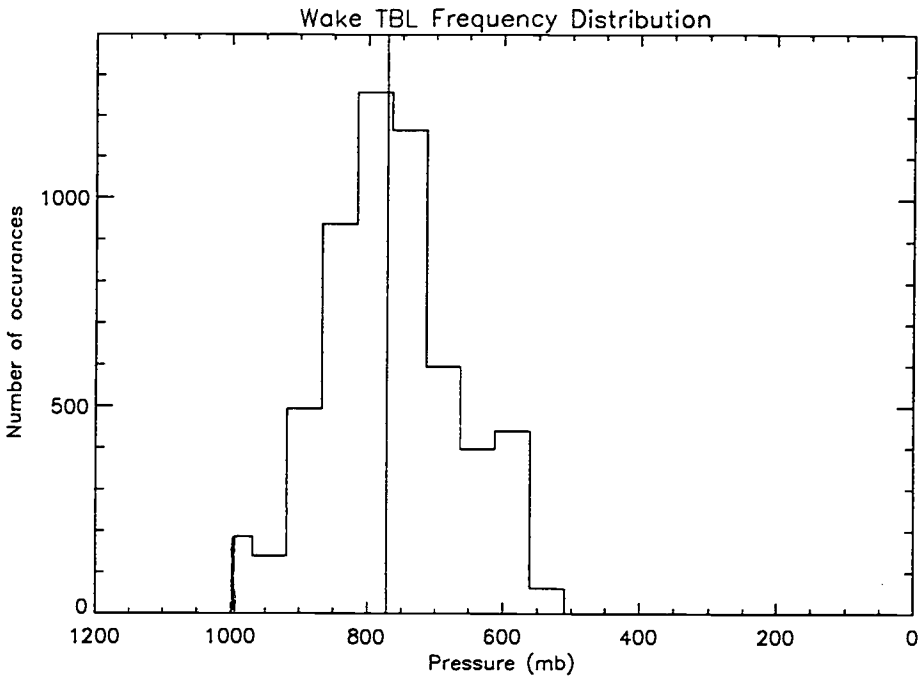

Figure 16 Wake TBL Frequency Histogram

After removing suspected outliers (those values outside of the three standard deviation interval about the mean) the mean and variance are recalculated. This procedure was repeated three times for each of the four methods. The resulting time series are relatively free of outliers and appear much 'cleaner'.

3.5 Spectral Analysis

Spectral analysis of a time series amounts to attempting to estimate the time series spectral density function. Fourier analysis seeks to approximate a function in terms of sines and cosines. A "well behaved" function, f(t), can be approximated by the Fourier series, where A_0 is a constant,

$$A_0 + \frac{1}{2\pi}\int_{-\pi}^{\pi} f(t)dt = \frac{1}{\pi}\sum_{r=1}^{k}\left(\left(\int_{-\pi}^{\pi} f(t)\cos\omega t\,dt\right)\cos\omega t\right) + \qquad (12)$$

$$\left(\left(\int_{-\pi}^{\pi} f(t) \sin \omega t dt \right) \sin \omega t \right)$$

which will converge to f(t) as k goes to infinity. Original attempts to discover hidden periodicities in a time series relied on computing Fourier series at all frequencies 2π/N, 4π/N,...π. A Fourier, or harmonic, analysis has N parameters to describe N observations and will fit the data exactly. Such an analysis depends on the assumptions that the time series is relatively stationary and that the sampling interval is constant. Analysis of evenly spaced time series tends to lead to the problem of aliasing.

The total energy of a function f(t) is given by

$$\int_{-\infty}^{\infty} |f(t)|^2 dt \tag{13}$$

where $|f(t)|^2$ is the instantaneous power of f(t).

By Parseval's theorem the total energy can be expressed as an integral over frequency

$$\int_{-\infty}^{\infty} |f(t)|^2 dt = \frac{1}{2\pi} \int_{-\infty}^{\infty} |f(\omega)|^2 d\omega \tag{14}$$

As applied to a truncated portion of the continuous function, f(t), the relation becomes

$$\int_{-\infty}^{\infty} |f(t)|^2 dt = \lim_{T \to \infty} \frac{1}{2\pi T} \int_{-T}^{T} |f(\omega)|^2 d\omega \tag{15}$$

where $\frac{|f(\omega)|^2}{T}$ is known as the periodogram. So $|f(\omega)|^2$ is the power (variance) per unit interval of frequency (Bath, 1974).

The basic tool for estimating power spectra of time series with N_0 discrete data points is the periodogram expressed in terms of the discrete Fourier transform,

$$P_x(\omega) = \frac{1}{N_0}\left[\left(\sum_{j=1}^{N_0} X_j sin\omega t_j\right)^2 + \left(\sum_{j=1}^{N_0} X_j \cos\omega t_j\right)^2\right] \qquad (16)$$

where X_j is the value of the time series f at time t_j. This form of the periodogram can be evaluated at any value of frequency, but traditionally this periodogram function is evaluated at a subset of $N_0/2$ evenly spaced frequencies (Scargle, 1982).

3.5.a Modified (Lomb) Periodogram

For the case of an unevenly sampled time series the periodogram must be modified in the following way,

$$P_x(\omega) = \frac{1}{2}\left\{\frac{\left[\sum_{j=1}^{N_0} X_j \cos\omega(t_j-\tau)\right]^2}{\sum_{j=1}^{N_0}\cos^2\omega(t_j-\tau)} + \frac{\left[\sum_{j=1}^{N_0} X_j \sin\omega(t_j-\tau)\right]^2}{\sum_{j=1}^{N_0}\sin^2\omega(t_j-\tau)}\right\} \qquad (17)$$

where τ satisfies the relation

$$\tan(2\omega\tau) = \frac{\left(\sum_{j=1}^{N_0}\sin 2\omega t_j\right)}{\left(\sum_{j=1}^{N_0}\cos 2\omega t_j\right)} \qquad (18)$$

This modified periodogram estimate of the power spectrum is equivalent to least-squares fitting of sinusoids to the data and has the added advantage of minimal aliasing due to the uneven sampling (Scargle, 1982).

3.5.b Spectral Analysis of TBL

An estimate of the power spectrum of TBL was created using a FT (Fourier Transform) modified periodogram method as discussed above. A large gap in the data set required the use of the Lomb periodogram method of calculating the FT sample power spectrum. The Lomb method evaluates the FT equations only at the points where there is a data value. A periodogram is calculated independent of shifting data points by a constant. Thus, the Lomb periodogram weights the data on a per point basis rather than on a per time basis. The resulting spectral estimate is similar to a spectrum calculated from a curve fitted to the irregularly spaced data (Scargle, 1982).

The null hypothesis for testing the significance level of a FT power spectrum peak is that data values are independent Gaussian random variables. Any value in the null hypothesis has an exponential probability distribution with a mean of one so that the probability, P, that a value is between z and z+dz is

$$P(z, z + dz) = e^{-z} dz \tag{19}$$

for M independent frequencies the probability of getting a value larger than z equation 22 becomes

$$P(> z) = 1 - \left(1 - e^{-z}\right)^{M} \tag{20}$$

For significance levels much less than 1 equation 23 reduces to

$$P(> z) \approx M e^{-z} \tag{21}$$

so that in terms of power units the significance can be expressed as

$$z = -\ln\left(\frac{P(>z)}{M}\right) \tag{22}$$

For this analysis M is chosen to be twice the number of data points in the original time series of the variable analyzed. If the data were equally distributed in time M would approach the number of data points. With uneven sampling the selection of M also depends on the rate of oversampling and the degree to which the data approach an even sampling rate (Press, 1992). Appendix A contains a discussion of testing performed on this spectra estimation algorithm for irregularly sampled known functions.

For example, if the significance level is chosen as 0.001 (99.9% confidence) and M is chosen as 5735 (the number of usable TBL data values for eight years of Wake data) the significance level in power units, z is 16.24. In this case every peak that is greater than 16.24 power units represents a real periodic signal at the corresponding frequency at the 0.001 significance level.

A filter based on the Haar transform (Mahrt and Howell, 1994) was applied to the spectral analysis results in order to reduce background noise for presentation purposes only. The Haar filter has the property of preserving edges so that peaks in the presented spectra are actually much sharper than the unfiltered spectra. Thus, peaks in the actual spectra are actually much broader than presented.

A similar analysis was performed on the boundary layer moisture parameter, Qdif, and on the ageostrophic parameter time series in order to better determine the behavior of the ageostrophic parameter in relationship to other boundary layer quantities.

Spectral analysis was applied to a 2.5° by 2.5° grid box of OLR data centered on the position 20° N 167.5° E. OLR is commonly used as a surrogate for deep convection, and has become a standard index of ISO activity. The OLR analysis will act as a reference for comparison with the results of the analyses performed on the other parameters.

Spectral analysis was also performed on the time series of the coefficients of the EOF modes of specific humidity profiles from Liu et al., (1991). In applications of EOF analysis, it is commonly the case that the different modes each represent a separate influence on the variance of the parameter studied, although it must be stated again that the mathematical orthogonality does not necessarily imply any physical or dynamical orthogonality. At the very least, the EOF analysis should have filtered out most of the background variance so that spectral analysis of the modes may be able to present a cleaner spectrum of specific humidity influences.

4. Results and Discussion

Table 1 shows a numerical breakdown of the sounding data by stratification and time of day. Stable conditions outnumber unstable conditions in all cases. The data are fairly evenly distributed between 12 GMT and 0 GMT with 0 GMT having fewer missing records. If all records possible for the period between January 1, 1980 and December 31, 1987 were present there would be 2922 individual days and 5844 total records.

Table 1 Numerical Breakdown by Stratification

Stratification	Total	12 GMT	0 GMT
Stable	4229	2271	1958
Unstable	1446	541	905
Total	5675	2812	2863

Simple linear regression analyses were performed to compare the output from the four boundary layer top diagnosis methods used. The model values for the PBL top were found to be in very good agreement with the direct data methods. Table 2 compares the regression correlation coefficients where the following definitions apply: BL is the boundary layer pressure time series derived from the temperature method, BLH is the time series of boundary layer top pressure that was found using the humidity jump detection method, WBL is the boundary layer top pressure time series based on the wind speed jump detection method, MBL is the time series of boundary layer top pressure that was calculated from the Richardson number

model, and TBL is the consensus "top of the boundary layer" pressure that arises from an intercomparison of the four diagnosis methods.

The correlation coefficients in table 2 are the result of comparisons over the eight years from 1980 to 1987. Table three gives an example of values for correlations performed on a single year (1982) time scale. In both cases the highest correlations (not including TBL) occur between MBL and BLH.

Table 2 Correlation Coefficients for PBL Top Determining Methods (Wake, 1980–87)

	TBL	BL	BLH	WBL	MBL
TBL		0.8822	0.9681	0.9069	0.9574
BL	0.8822		0.8509	0.8462	0.9138
BLH	0.9681	0.8509		0.8754	0.9420
WBL	0.9069	0.8462	0.8754		0.9299
MBL	0.9574	0.9138	0.9420	0.9299	

The correlations hold to the same pattern for 0 GMT and 12 GMT with slight changes in the magnitudes of the correlation coefficients (tables 4 and 5). The reason for the better agreement between the Richardson number model (MBL) and the humidity detection method (BLH) is that the Richardson number model contains virtual potential temperature, Θ_v, which should include boundary layer humidity effects.

By examining the coefficients in table 2, one can estimate the impact of ignoring the water vapor influence on buoyancy in the determination of the PBL top. The model method has a correlation coefficient with the temperature method

of 0.91. The coefficient with the humidity method is 0.942. When Θ_v, is used in the temperature method, the coefficient with the model method goes up to nearly that of the humidity method value. Thus, the humidity method identifies approximately 3% more boundary layer tops than the temperature method.

TBL is the value of the PBL top pressure that is chosen by comparing the values of the four methods. When two or more of the methods result in the same PBL top pressure, that value becomes the consensus "top of the boundary layer" pressure, or TBL. It is the time series of TBL that gives the boundary layer height from which the geostrophic wind speed is defined.

In the case that no two of the four methods agree on a PBL top pressure, the TBL value is set to the BLH value since BLH has the highest correlation coefficients with the other methods.

Table 3 Correlation Coefficients for PBL Top Determining Methods (Wake, 1982)

	TBL	BL	BLH	WBL	MBL
TBL		0.8013	0.9618	0.8773	0.9509
BL	0.8013		0.7782	0.7542	0.8287
BLH	0.9618	0.7782		0.8451	0.9213
WBL	0.8773	0.7542	0.8451		0.9036
MBL	0.9509	0.8287	0.9213	0.9036	

Table 4 Correlation Coefficients for PBL Top Determining Methods 12 GMT (Wake, 1980–87)

	TBL	BL	BLH	WBL	MBL
TBL		0.8883	0.9756	0.9192	0.9718
BL	0.8883		0.8644	0.8555	0.9181
BLH	0.9756	0.8644		0.8945	0.9522
WBL	0.9192	0.8555	0.8945		0.9359
MBL	0.9718	0.9181	0.9522	0.9359	

Table 5 Correlation Coefficients for PBL Top Determining Methods 0 GMT (Wake, 1980–87)

	TBL	BL	BLH	WBL	MBL
TBL		0.8752	0.9643	0.9000	0.9655
BL	0.8752		0.8426	0.8414	0.9102
BLH	0.9643	0.8426		0.8653	0.9357
WBL	0.9000	0.8414	0.8653		0.9297
MBL	0.9655	0.9102	0.9357	0.9297	

4.1 Comparisons by Stratification and Time of Measurement

The data can be further broken down in terms of static stability and time of measurement. Tables 6–9 show correlation coefficients for each of the four data divisions. Correlation coefficient values are in general higher for the nighttime (12 GMT) cases.

Correlations with TBL for the nighttime (12 GMT) cases show higher values for the stable case than for the unstable case. The correlations with TBL for the

daytime (0 GMT) cases show higher values for the stable cases with BL and WBL and lower values for the stable cases with MBL and BLH.

Table 6 Correlation Coefficients for PBL Top Determining Methods, Stable 12 GMT (Wake, 1980–87)

	TBL	BL	BLH	WBL	MBL
TBL		0.8221	0.9474	0.8548	0.9479
BL	0.8221		0.7751	0.7648	0.8689
BLH	0.9474	0.7751		0.8120	0.9116
WBL	0.8548	0.7648	0.8120		0.8856
MBL	0.9479	0.8689	0.9116	0.8856	

Table 7 Correlation Coefficients for PBL Top Determining Methods, Unstable 12 GMT (Wake, 1980–87)

	TBL	BL	BLH	WBL	MBL
TBL		0.8040	0.9217	0.8502	0.9195
BL	0.8040		0.7779	0.7734	0.8715
BLH	0.9217	0.7779		0.8048	0.8951
WBL	0.8502	0.7734	0.8048		0.8845
MBL	0.9195	0.8715	0.8951	0.8845	

Table 8 Correlation Coefficients for PBL Top Determining Methods, Stable 0 GMT (Wake, 1980–87)

	TBL	BL	BLH	WBL	MBL
TBL		0.8085	0.9318	0.8395	0.9365
BL	0.8085		0.7534	0.7632	0.8630
BLH	0.9318	0.7534		0.7807	0.8830
WBL	0.8395	0.7632	0.7807		0.8925
MBL	0.9365	0.8630	0.8830	0.8925	

Table 9 Correlation Coefficients for PBL Top Determining Methods, Unstable 0 GMT (Wake, 1980–87)

	TBL	BL	BLH	WBL	MBL
TBL		0.7995	0.9412	0.8292	0.9378
BL	0.7995		0.7618	0.7541	0.8663
BLH	0.9412	0.7618		0.7893	0.9027
WBL	0.8292	0.7541	0.7893		0.8805
MBL	0.9378	0.8663	0.9027	0.8805	

A student's t-test was performed on the difference of means for each of the combinations of methods (BL, MBL, WBL, BLH) with TBL for each of the four divisions (0 GMT/12 GMT, stable/unstable). Table 10 shows sample statistics for these comparisons. The results of table 10 suggest that a comparison of the means of the distributions of the four methods of boundary layer top diagnosis are not significantly different from the mean of TBL to a confidence level of 99%. Therefore it is reasonable to assume that the distribution of TBL adequately represents the distributions of the each of the four diagnosis methods.

Table 10 Sample Statistical Tests on PBL Top Diagnosis Methods with TBL 12 GMT Unstable. TBL Mean M1=770.7, s=88.5

Method	Mean (M2) mb	N	Standard Deviation	Test stat.	H_0: M1=M2	Confid. Level %
BL	758.9	541	105.9	2.0	accept	99.0
MBL	765.4	541	90.3	0.99	accept	99.0
WBL	783.9	541	104.0	-2.2	accept	99.0
BLH	778.3	541	89.8	-1.39	accept	99.0

4.2 Spectral Analysis Results

A spectral analysis based on the Fourier transform was performed on the complete TBL time series to find the frequencies that contribute most to the variance of the time series. Frequencies with a power value larger than 16 are significant contributors to the variance of the time series. In all figures representing estimates of spectra the dotted line represents the 0.001 significance level, the dashed line indicates the 0.005 significance level, and the dash-dot line represents the 0.05 significance level for the time series analyzed. Thus a peak that has a power above the dotted line, for example, is said to be statistically significant to a confidence level of 99.9%. In the cases where filtered power spectra are presented, an estimated 0.001 significance level is shown as a dotted line.

With the exception of the missing data in the ageostrophic time series, the sampling rate of all the time series are very nearly uniform. The modified (Lomb) periodogram is designed for unevenly sampled time series which presumably reduces aliasing problems (Scargle, 1982). Since it is the uneven sampling rate,

and not the modified periodogram itself, that minimizes aliasing, it is reasonable to assume that some aliasing occurs when the modified periodogram is applied to nearly evenly sampled time series.

If this is the case, removal of the estimated annual cycle via calendar day averaging should also remove the harmonics (integer multiples of the annual frequency) with periods of 180 days and 120 days when deviations spectra are calculated. The modified periodogram method was chosen for this analysis for its ability to accommodate the large gap in wind data, rather than for its uneven sampling rate benefits.

4.2.a OLR Spectral Analysis Results

The spectrum of outgoing longwave radiation (OLR), figure 17, shows a strong peak at the annual cycle frequency and at the 180 day harmonic. One very strong peak in the ISO range occurs at a period of about 38 days. An estimated annual cycle, comprised of an eight-year-calendar-day average, was removed from the data and the resulting deviations spectrum appears in figure 18.

The estimated annual cycle seems to have adequately remove the power at the annual frequency and its harmonics as evidenced by the lack of a peak a the annual frequency of 0.0028 1/day in the deviations spectrum (figure 18). The strong peak in the ISO range is significant to the 0.001 level and has a period of approximately 38 days.

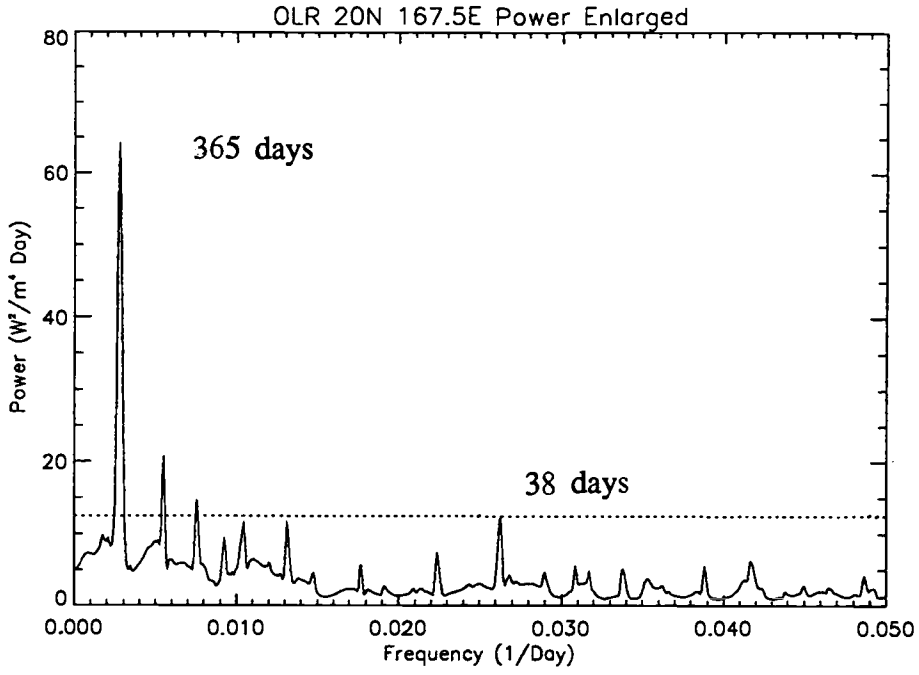

Figure 17 Nighttime OLR 20 °N 167.5 °E Filtered Sample Power Spectrum

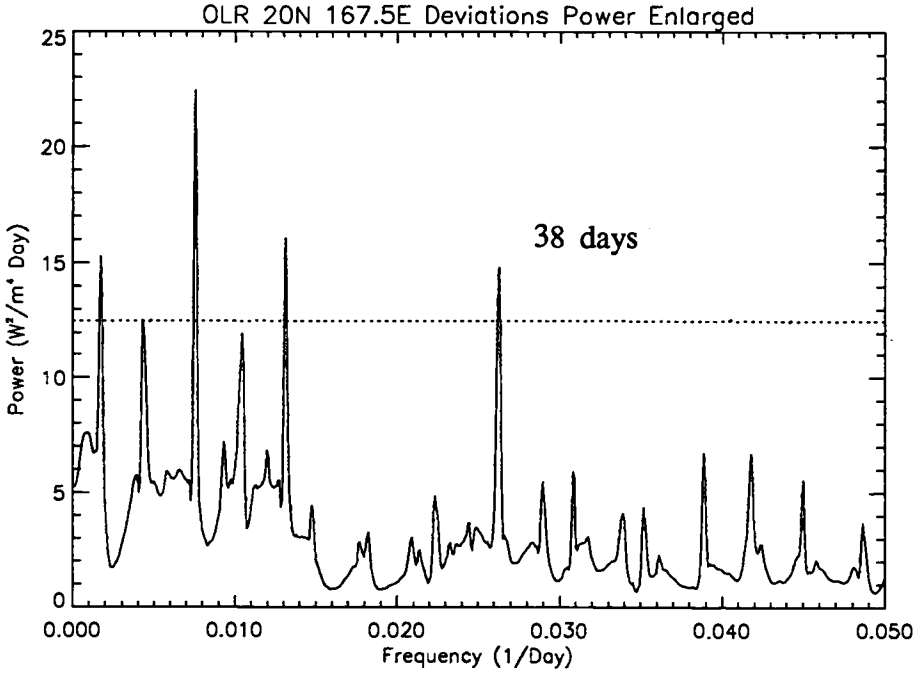

Figure 18 Nighttime OLR 20 °N 167.5 °E
Deviations Filtered Sample Power Spectrum

4.2.b The Annual Cycle

The sample spectrum of boundary layer top shown in figure 19 shows a dominant peak near the 1 cycle per 365 days frequency. With peak power at a frequency of 0.0028 1/day (period of 356 days). Another significant (0.001 significance level) peak occurs at a frequency of 0.0055 1/day (period of about 180 days).

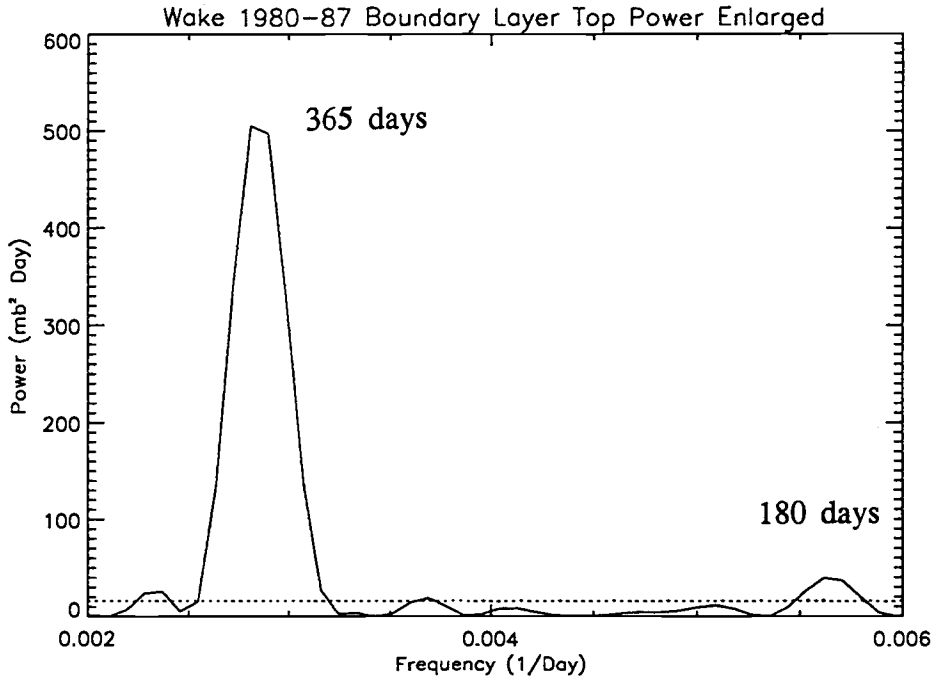

Figure 19 Wake TBL Sample Power Spectrum

The Qdif spectrum and ageostrophic parameter spectrum are very similar to the spectrum of boundary layer top. All three spectra are dominated by a single peak corresponding to frequencies of the annual cycle. The Qdif spectrum is dominated by a peak ranging from 0.00279–0.00317 1/day (range of periods from

315–357 days); peak power occurs at a frequency of 0.0029 1/day (period of about 335 days).

The ageostrophic parameter spectrum (figure 20) shows a strong peak corresponding to the annual cycle peak corresponding to frequencies from 0.00264–0.00291 1/day (periods ranging from 343–377 days).

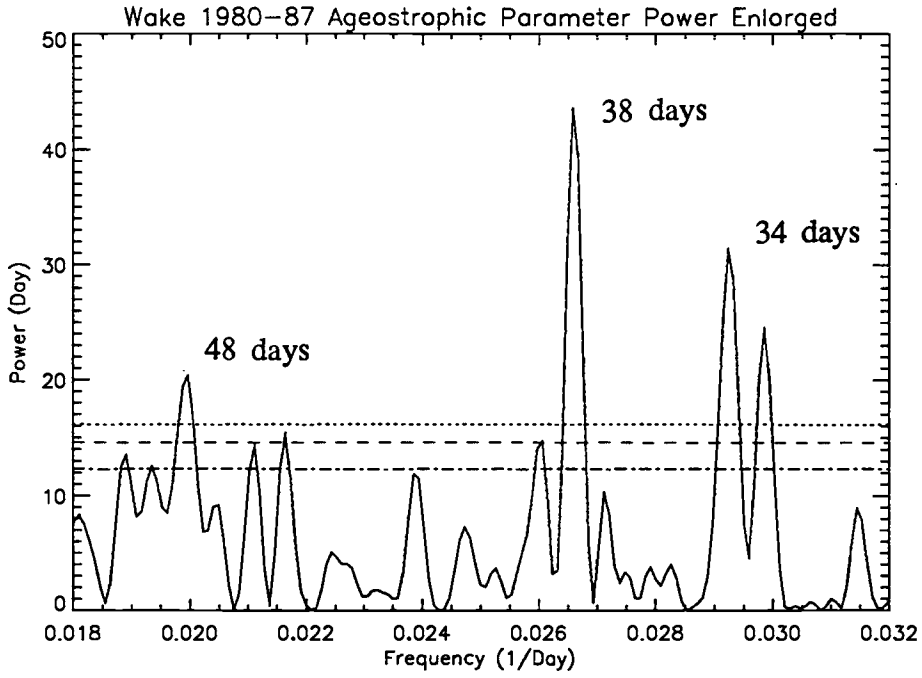

Figure 20 Wake Ageostrophic Parameter Sample Power Spectrum

Spectral estimates of the EOF modes of specific humidity from Liu et al., (1991) show strong 1 cycle per 365 days peaks in each of the three modes. The mode 1 spectrum is dominated by the annual cycle as shown in figure 21. In addition to the annual cycle peak, a peak occurs at 0.0054 1/day (period of about 180 days). Spectra of EOF modes of specific humidity two and three are similarly dominated by the annual cycle peak.

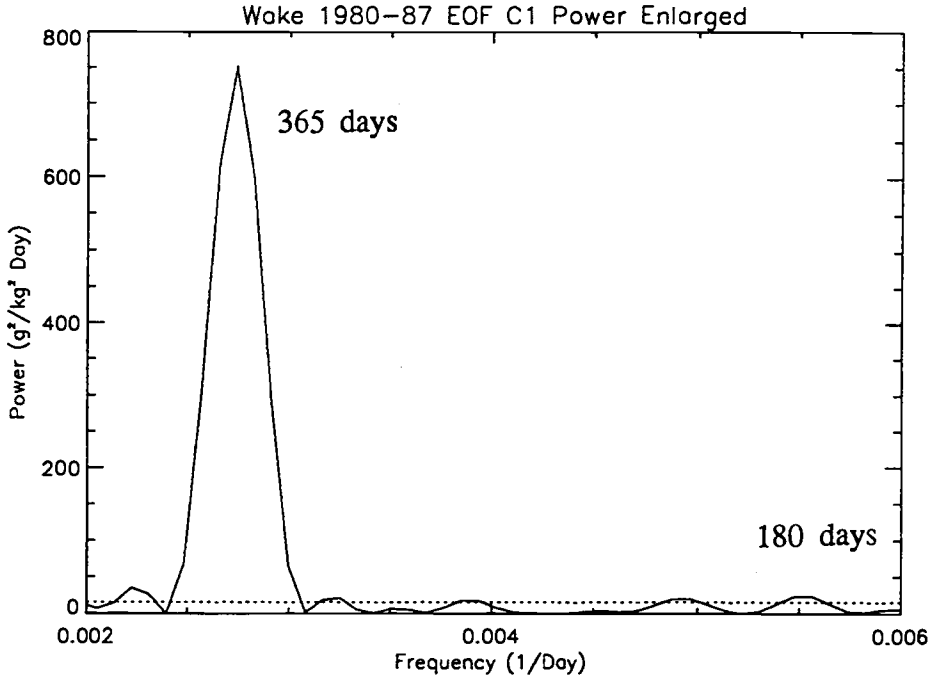

Figure 21 Enlarged EOF Mode 1 (C1) Sample Power Spectrum

4.2.d Removal of the Annual Cycle

An estimate of the annual cycle was removed from of the time series by subtracting an eight-year-calendar-day-average from the corresponding parameter's time series value.

The EOF modes of specific humidity profiles for Liu et al., (1991) were used to represent the most important processes affecting boundary layer humidity. The information in these modes should all be contained in the time series of the parameter Qdif. Analysis of Qdif was hindered by a large amount of noise in the time series data. The EOF modes of specific humidity have the advantage that background noise was filtered out during the EOF analysis.

For all three EOF modes of specific humidity the calendar day averaging scheme was successful in removing the annual cycle and its harmonics as indicated by the lack of annual peaks in the deviations spectra.

The removal of the eight-year-calendar-day-average shows up in the boundary layer top deviations spectrum as a strong reduction of power at 0.0028 1/day (period of 356 days). The spectrum is now dominated by a peak at the frequency 0.0029 1/day (period of about 343 days) similar to the main peak in the Qdif spectrum. A peak at 0.0055 1/day (period of about 180 days) is above the 0.001 significance level.

As in the TBL analysis an estimated annual cycle of Qdif was calculated by a calendar day average. Deviations time series of Qdif were calculated by subtracting this estimated annual cycle from the original time series data.

Power spectra estimates of Qdif deviations give results similar to those for TBL deviations. The daytime (0 GMT) spectrum shows a single dominant peak corresponding to the 1 cycle per 365 days frequency and a secondary peak corresponding to a period of 6 months. The nighttime (12 GMT) deviations spectrum shows the power distributed over many frequencies and a depressed 1 cycle per 365 days peak. None of the nighttime (12 GMT) Qdif deviations peaks are statistically significant.

The Qdif deviations spectrum indicates a continued strong annual cycle peak in the range of 0.0026–0.0028 1/day (periods from 354–377 days). A peak significant to the 99.5% confidence level occurs at a frequency of 0.0055 1/day (period of about 180 days).

The ageostrophic parameter deviations spectrum indicates a drop in power in the annual cycle range but still retains a significant peak in the range 0.0025–0.0027 1/day (365–377 day period range).

Table 11, where a "d" indicates the time series of deviations from the eight-year-calendar-day-average of the parameter, shows that removal of the estimated annual cycle from the combined 12 GMT/ 0 GMT time series was not successful. Although some of the power associated with the annual cycle and its harmonics was removed through averaging, the overall effect of removing the eight-year-calendar-day-average on the power spectra was minimal.

Table 11 Summary of Periods Corresponding to the Annual Cycle

Period	TBL	dTBL	Qdif	dQdif	Ageo	dAgeo
Yearly (Max.)	325-379 (356)	324-376 (365)	306-357 (335)	307-376 (365)	333-377 (353)	365-377 (376)
180 day	175-180	177-185	none	177-179	none	none
120 day	128	129	none	none	117-125	121-125

A similar problem with removal of the annual cycle was attributed to the annual cycle having interannual variations in amplitude and phase (Hartmann and Gross, 1988). In order to understand why the removal of the estimated annual cycle failed, the time series must be broken up into separate 12 GMT and 0 GMT series.

4.2.e Diurnal Difference in Persistence of Annual Cycle

The power spectra for the boundary layer top time series for both 0 GMT and 12 GMT are similar to figure 19. Both spectra are dominated by a single large peak corresponding to the annual cycle.

An estimated annual cycle was removed from both the 0 GMT and 12 GMT time series in order to determine other periodicities in the time series that might have been overshadowed by the extremely dominant annual cycle and to gain some insight as to why the annual cycle continues to persist in the deviations of the combined time series. The data were averaged by calendar day and removed from the original time series. The eight-year-calendar-day-mean was then subtracted from the original time series to create the time series of deviations.

Figures 22 and 24 show plots of the filtered time series of boundary layer top pressure level with the estimated annual cycle removed for nighttime (12 GMT) and daytime (0 GMT) respectively. The nighttime (12 GMT) spectrum, figure 23, shows the power distributed over many frequencies and no significant peak at 1 cycle per 365 days but a strong peak is located at 0.0029 1/day (period of 333 days).

The daytime (0 GMT) boundary layer top spectrum, figure 25, shows a dominant peak at the 1 cycle per 365 days frequency and at 0.0054 1/day (period of about 182 days) with power significant to the 0.001 level.

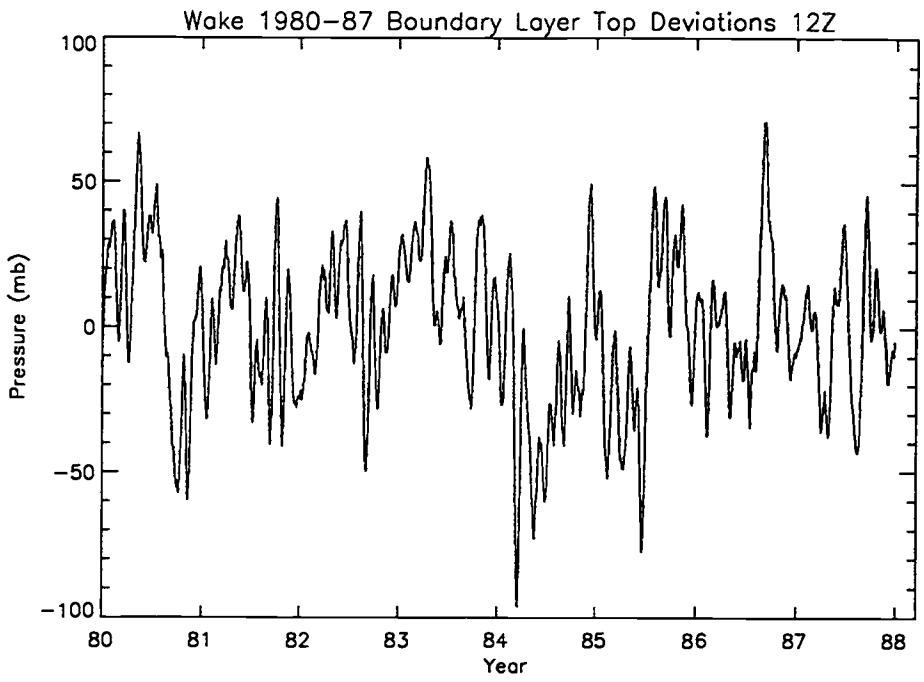

Figure 22 Wake Filtered TBL Deviations Time Series, 12 GMT

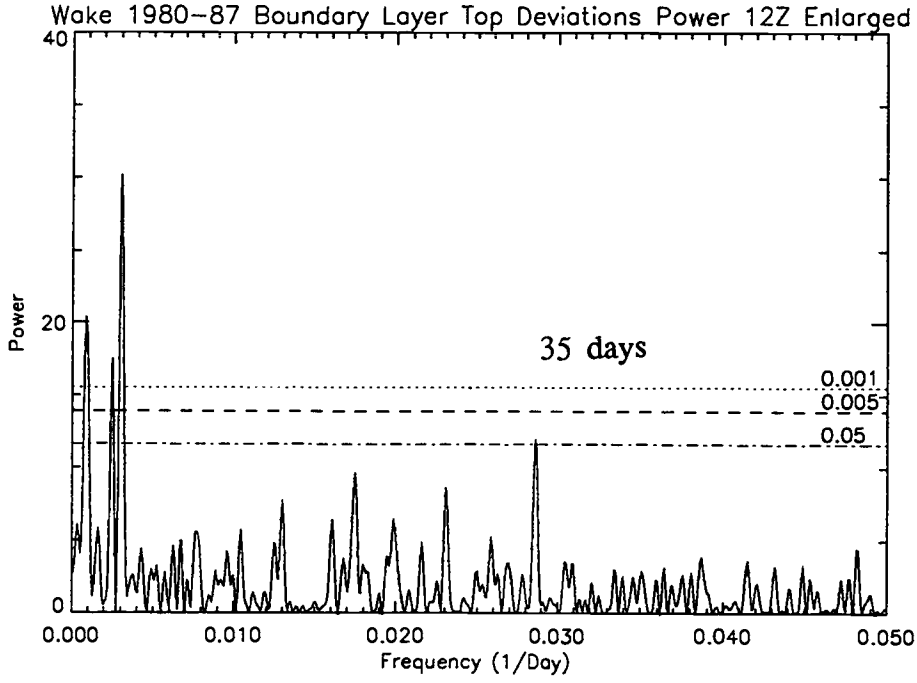

Figure 23 Enlarged Wake TBL Deviations 12 GMT Sample Power Spectrum

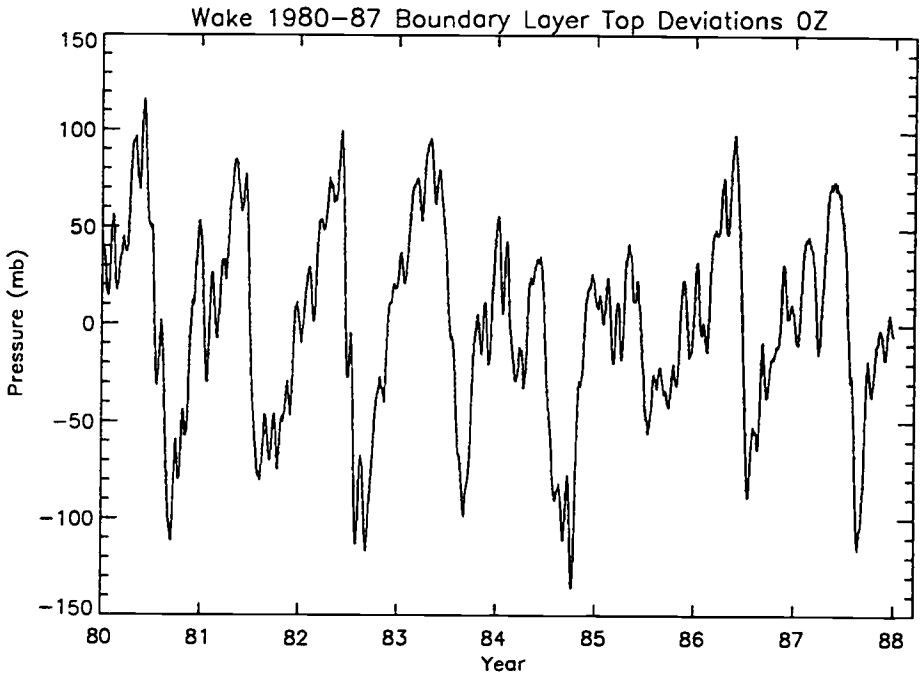

Figure 24 Wake Filtered TBL Deviations Time Series, 0 GMT

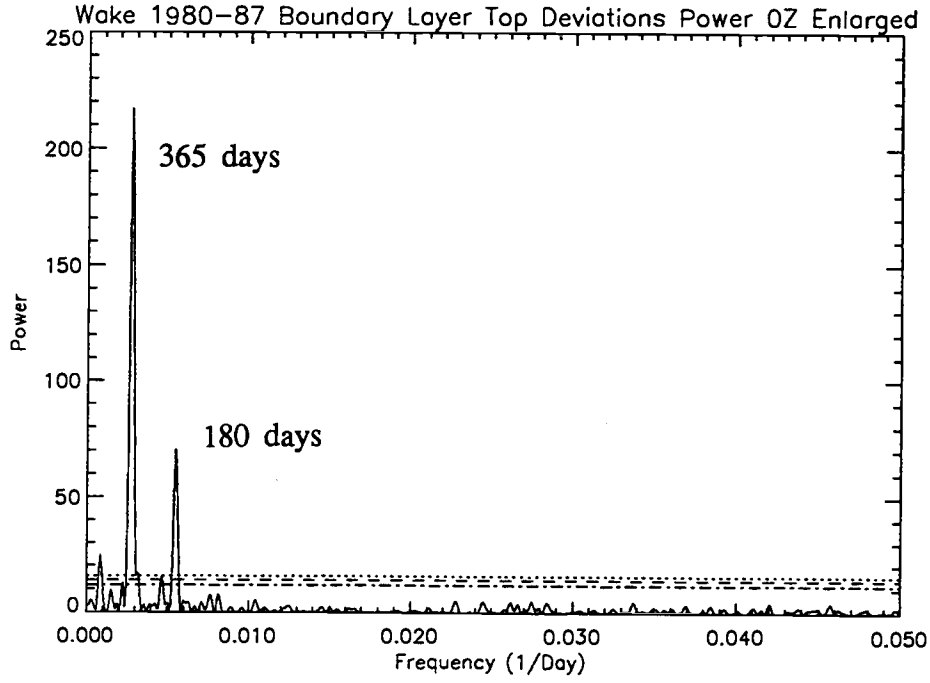

Figure 25 Enlarged Wake TBL Deviations 0 GMT Sample Power Spectrum

This pattern of an absent annual cycle peak in the nighttime (12 GMT) deviations spectrum while a strong annual peak dominates the daytime (0 GMT) deviations spectrum, is repeated in the Qdif parameter and in the ageostrophic parameter spectra.

Both the daytime (0 GMT) and the nighttime (12 GMT) ageostrophic parameter spectra show an annual cycle peak. Calendar day averages were calculated to create an estimated annual cycle. The calendar day averages were subtracted from the original ageostrophic parameter time series to form a time series of ageostrophic parameter deviations for both 12 GMT and 0 GMT.

The nighttime (12 GMT) ageostrophic parameter deviations spectrum has no significant peaks associated with the annual cycle. The daytime (0 GMT) spectrum of the ageostrophic parameter deviations time series still shows a large peak corresponding to the 1 cycle per 365 days frequency and a peak significant to the 0.001 level at 0.0082 1/day (period of about 120 days).

Table 12 shows a comparison by common periods of the ageostrophic parameter spectra with the spectra of ageostrophic parameter deviations for both 12 GMT and 0 GMT. A "yes" in table 12 indicates a significant peak is present in the spectrum, and a "no" indicates the lack of a significant peak. In the nighttime (12 GMT) case, the periods corresponding to the annual cycle and its harmonics do not show up in the spectrum of the deviations series. The daytime (0 GMT) case, however, indicates that annual cycle and its harmonics have not been removed from the deviations spectrum by the calendar day averaging.

Table 12 Summary of Comparison Between Ageo and dAgeo Common Periods

Period (days)	12 GMT	d 12 GMT	0 GMT	d 0 GMT
365	yes	no	yes	yes
124	yes	no	yes	yes
48	yes	yes	yes	yes
38	yes	yes	yes	no
34	yes	yes	yes	yes
26	yes	yes	yes	yes

Since the combined time series of the parameters contained the daytime (0 GMT) information, it was impossible to remove the annual cycle from the original time series. Thus, periods corresponding to the annual cycle and its harmonics were not removed by the calendar day averaging process applied to the original time series, but were removed successfully from the nighttime (12 GMT) deviations series.

The difference between the daytime (0 GMT) spectra and the nighttime (12 GMT) spectra is also reflected in the surface level variance of specific humidity. Using the components of Qdif, table 13 shows the boundary layer level difference in specific humidity variance between daytime (0 GMT) and nighttime (12 GMT) is quite small. The daytime (0 GMT) surface level variance of specific humidity is over three times the surface level variance of the nighttime (12 GMT) specific humidity.

Table 13 Comparison of Diurnal Specific Humidity Variance

Specific Humidity	0 GMT Variance	12 GMT Variance
Surface (Qs)	20.235	6.163
Boundary Layer (Qb)	12.482	14.069

This large difference in variance could be related to the fact that Wake is an island station. The variance of the surface specific humidity could be strongly influenced by daytime heating and subsequent convection near the surface. The daytime heating could also affect the ageostrophic parameter via increased gustiness of the surface wind. Daytime heating would be active near 0 GMT (noon local time) and would also be strongly dependent on the annual cycle (i.e. ITCZ migration). Daytime heating of the island surface would not be expected to alter the variance at the boundary layer level since the nature of a radiosonde balloon is to travel with the wind and would thus no longer be over the island upon reaching the boundary layer height. Thus, daytime heating does not explain why the annual cycle persists in the daytime (0 GMT) boundary layer top.

Another possible explanation for the persistence of the annual cycle in the daytime spectra is that the data may contain a period of increased amplitude that could allow the annual cycle to persist. One month or season of extremely abnormal data may remain after the eight-year-calendar-day averaging estimated annual cycle is removed, thus causing the annual cycle to persist. A prime candidate for this skewed amplitude would be during the strong ENSO event in 1983 where the time series of the parameters studied here exhibit different

characteristics that are visible to the naked eye. However, attempts to test this theory have thus far been inconclusive. It is also not clear as to why interannual variability contamination should show a diurnal difference in character.

Since the cause of the daytime annual cycle persistence is not easily identified, the comparisons for the rest of this analysis were performed on the nighttime (12 GMT) data and spectra.

4.2.f ISO range results

The spectrum of OLR deviations (figure 26) from the estimated annual cycle shows a single dominant peak in the ISO range (30–60 days period) at a period of about 38 days. The 38 day peak is significant to the 0.001 level before filtering.

In the ISO range of the TBL deviations spectrum there is one peak, shown in figure 27, at a frequency of 0.0285 1/day (period of about 35 days) that is only significant to the 0.08 level (or 92% confidence level).

Significant (all better than 0.001 significance level) peaks in the ageostrophic parameter spectrum corresponding to the ISO frequency range include: a peak at 0.0208 1/day (48 days period), a strong peak at a frequency of 0.0265 1/day (period of about 37 days), and a peak at 0.0292 1/day (period of 34 days).

Peaks significant to the 0.001 significance level in the spectrum of ageostrophic parameter deviations corresponding to the ISO range include: 0.0207 1/day (period of about 48 days), 0.0262 1/day (period of about 38 days), and 0.0293 1/day (period of about 34 days).

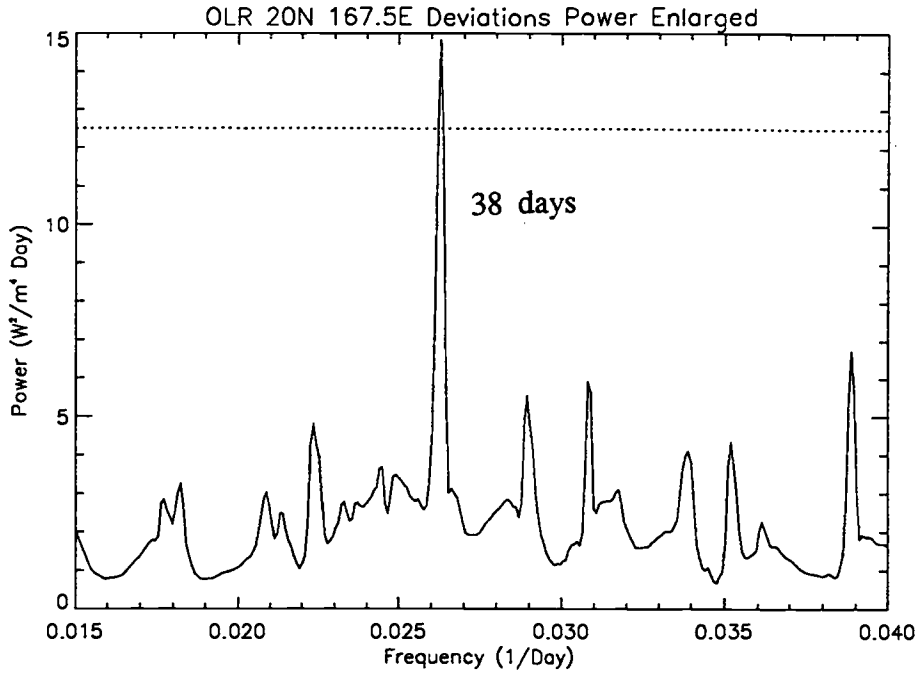

Figure 26 Nighttime OLR 20 °N 167.5 °E
Deviations Filtered Sample Power Spectrum

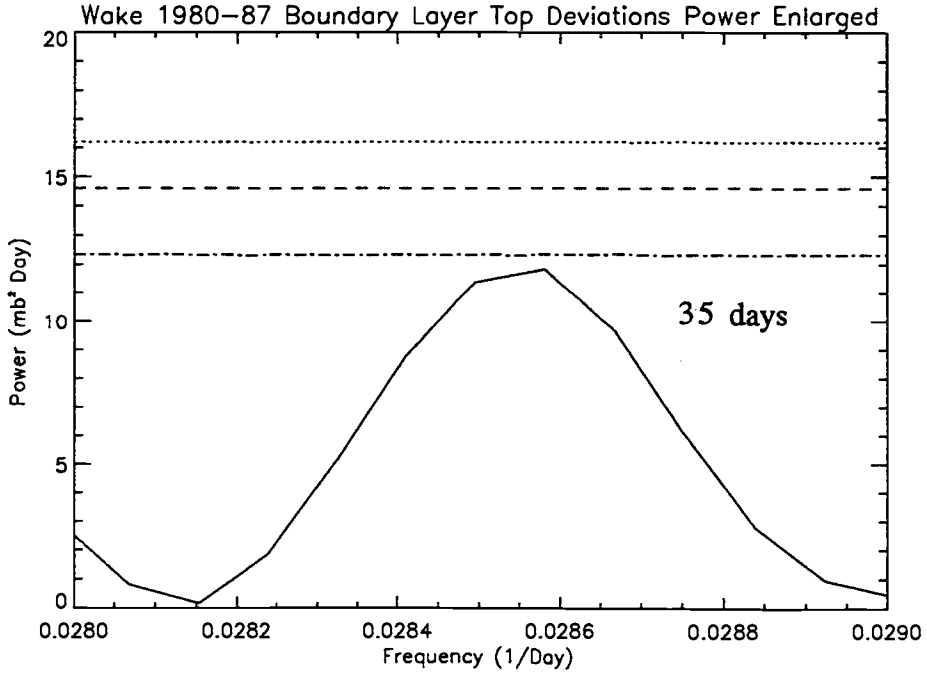

Figure 27 Enlarged Wake TBL Deviations Sample Power Spectrum

In the ISO range of the TBL nighttime (12 GMT) spectrum, a peak at frequency 0.0285 1/day (period of about 35 days) is significant to the 0.05 level.

The nighttime (12 GMT) ageostrophic parameter deviations spectrum (shown in figure 28) has peaks significant to the 0.001 level at: 0.0207 1/day (period of about 48 days), 0.0261 1/day (period of about 38 days). A peak significant to the 0.005 level occurs at 0.0287 1/day (period of about 34 days).

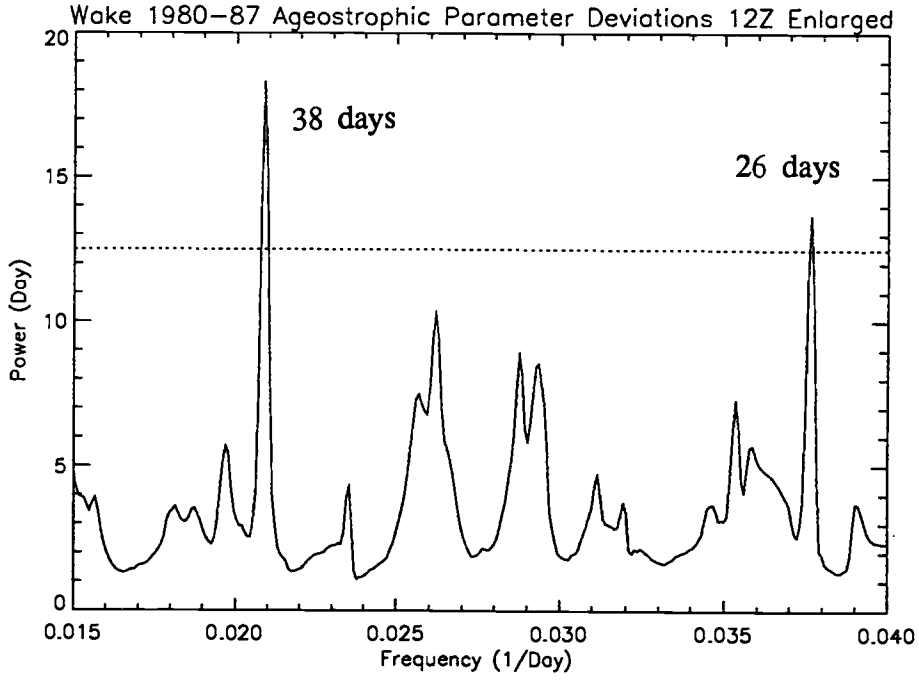

Figure 28 Enlarged Wake Ageostrophic Parameter Deviations Filtered 12 GMT Sample Power Spectrum

Figure 29 shows the spectrum of deviations from the eight-year-calendar-day-average of the first EOF mode of specific humidity, which has peaks significant to the 0.001 level at frequencies of 0.0262 1/day (period of about 38 days) and 0.0336 1/day (period of about 30 days). The second mode deviations spectrum does not show significant peaks in the ISO range of periods. The third mode

deviations spectrum shows a peak in the ISO range with a significance of 0.1 with maximum power at 0.0208 1/day (period of about 47 days).

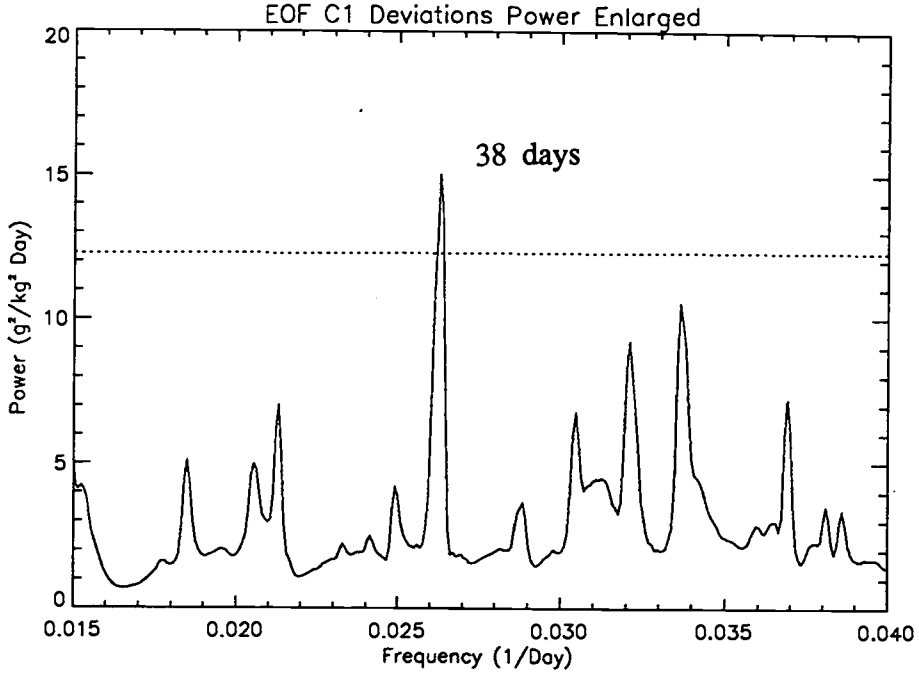

Figure 29 Enlarged EOF Mode 1 (C1)
Deviations Filtered Sample Power Spectrum

4.2.g Other Significant Peaks

The predominance of low frequency peaks in the ageostrophic parameter spectra estimates indicates that the ageostrophic parameter time series has periodicities on time periods longer than the data record. Since this study only covered eight years of data it was not possible to examine anything but the trends of the lower frequency influences that occurred during the data period. The overall trend over the eight years of ageostrophic parameter data was a general decrease in values

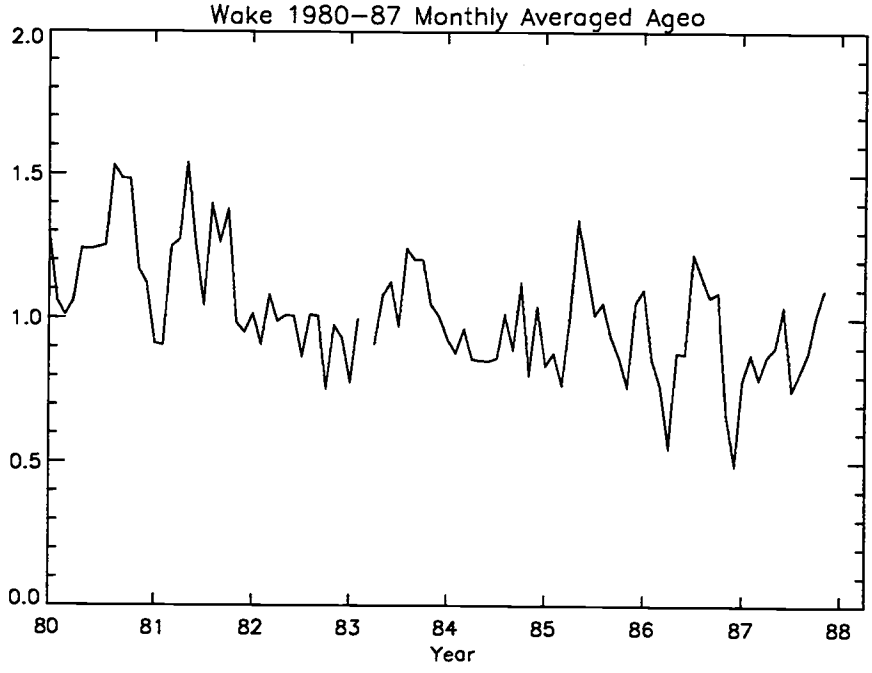

Figure 30 Wake 1980–87 Monthly Averaged Ageostrophic Parameter

with increasing time as shown in figure 30. Note the visibly strong reduction in variance during the ENSO event of 1982–83.

Another significant peak in the ageostrophic parameter deviations spectrum occurs just outside the ISO range at a frequency of 0.0385 1/day (period of about 26 days).

4.2.h Discussion of ISO range results

Table 14 shows significant peaks occurring in the ISO range of periods (30–60 days) in the spectra of nighttime OLR, nighttime (12 GMT) boundary layer deviations, nighttime (12 GMT) deviations of the ageostrophic parameter, and in the deviations spectra of the first and third EOF modes of specific humidity.

Table 14 Summary of Comparison Between Deviation Spectra Common Periods in the ISO Range

Period (days)	dOLR	dTBL 12	dAgeo 12	dC1	dC2	dC3
48			yes			yes
38	yes		yes	yes		
34		yes	yes			

The third EOF mode deviations spectrum and the ageostrophic parameter deviations spectrum both show a peak at a period of 48 days. The ageostrophic parameter peak is significant to the 0.005 significance level, while the EOF mode 3 peak is only significant to the 0.1 level.

The first EOF mode deviations spectrum, the OLR deviations spectrum, and the ageostrophic parameter deviations spectrum all show a significant peak corresponding to a period of 38 days. Both the OLR and EOF mode 1 peaks have a significance level of 0.001, while the ageostrophic parameter peak is only significant to the 0.05 level.

Both the ageostrophic parameter deviations spectrum and the spectrum of nighttime (12 GMT) boundary layer top deviations show a peak at a period of 34 days. In the case of the boundary layer top deviations spectrum, this peak is only significant to the 0.05 level. The significance level of both the ageostrophic parameter deviations peaks is 0.005. None of the EOF mode deviations show a significant peak at a period of 34 days.

The common frequencies between the 12 GMT ageostrophic parameter deviations spectrum, the 12 GMT boundary layer top deviations spectrum, and the deviations of the first and third EOF modes of specific humidity spectra in the ISO range, suggest that the ageostrophic parameter may represent a physical process common to both the dynamics and the humidity in the ISO frequency range. This relationship may be important since recent modelling evidence (e.g. Goswami and Shukla, 1984, Cho et al., 1994) and observational evidence from Lau and Chan, (1985) have indicated that the 40–50 day oscillation may actually be an interaction between dynamics and condensational heating.

Significant peaks of approximately 26 days period were observed in the ageostrophic parameter spectra and may lend observational evidence to peaks with shorter periods (20–30 days) presented in results of model simulations (Lau and Chang, 1992, Ghil and Mo, 1991, and Hartmann, et al., 1992).

Two peaks significant to the 0.05 level occur in the spectrum of deviations of the daytime (12 GMT) ageostrophic parameter at periods of 48 days and 38 days. These two peaks do not correspond to significant peaks in either the deviations of the boundary layer top. The 48 day and 38 day peaks in the ageostrophic parameter deviations spectrum may reflect the seasonality of the change in magnitude of the 40–50 day spectral peak.

4.2.i Seasonality of the 40–50 Day Peak

Since the ageostrophic parameter deviations spectrum contains information throughout the year, it seems possible that the 38 day and 48 day peaks may

represent the spring and winter/summer changes in period. Figure 31 shows a power spectrum estimate calculated from ageostrophic parameter data composed from the eight years of data for the month of May. The dominant peak in the ISO range is centered around the frequency 0.020 1/day (period of 50 days). A similar spectrum calculated for a composite December is shown in figure 32. The main ISO range peak, in this case, has its center at a frequency of 0.024 1/day (period of about 41 days). This supports the shift in period between early NH spring and late NH winter reported by Hartmann et al., (1992).

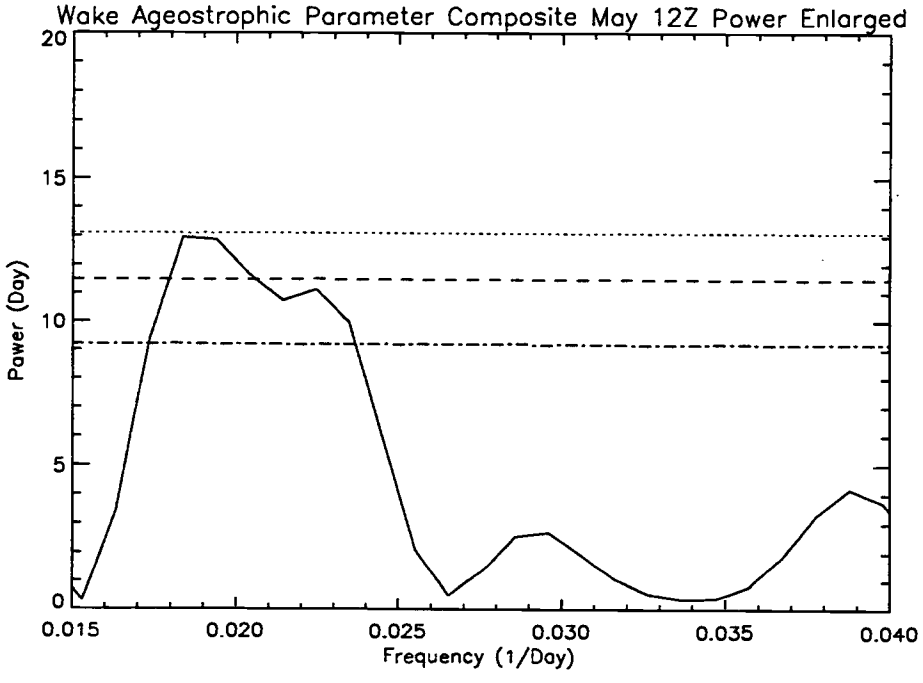

Figure 31 Wake Composite-May Ageostrophic Parameter Sample Power Spectrum

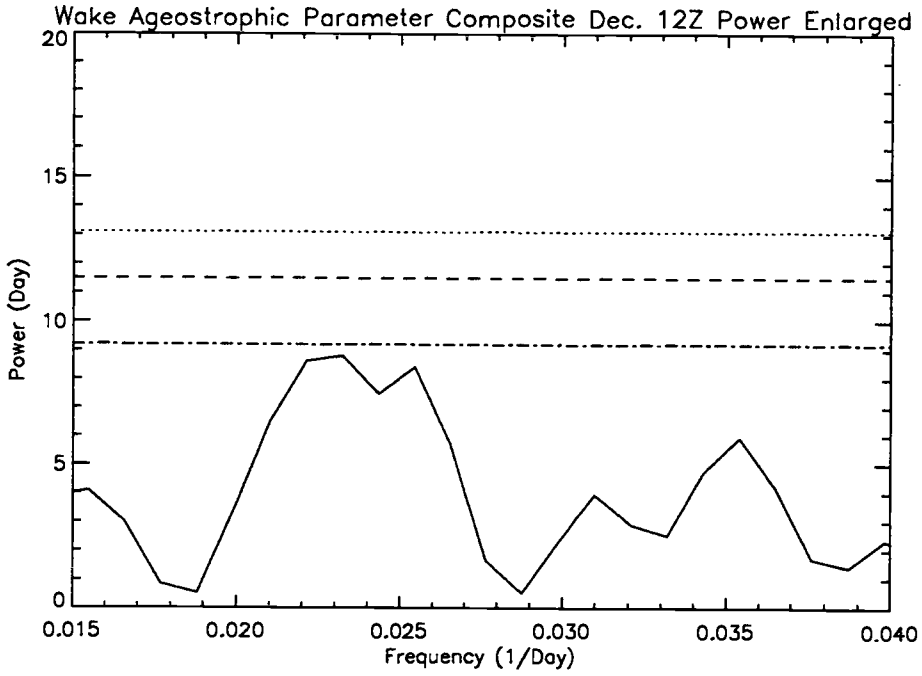

Figure 32 Wake Composite-December
Ageostrophic Parameter Sample Power Spectrum

5. Conclusions

Eight years of high-resolution rawinsonde data were analyzed to examine the characteristics of the ageostrophic parameter and its relationship to tropical boundary layer processes. A time series of boundary layer top was constructed from the data using a PBL top diagnosis algorithm. Results of the PBL top time series obtained from the three diagnosis methods were compared to results obtained from a Richardson number model of PBL top and were found to agree with the direct data methods. Correlation coefficients between the direct data methods and the model method were all above 0.91 with the nighttime (12 GMT) values slightly higher than those for daytime (0 GMT).

Spectral analysis was performed on the time series of boundary layer top, the ageostrophic parameter, and a boundary layer humidity parameter. The results show that the annual cycle dominates the spectra of all three parameters. The attempt to remove the estimated annual cycle from the time series of the three parameters was successful for the nighttime (12 GMT) cases but not the daytime (0 GMT) cases. A large diurnal difference in the variance of specific humidity at the surface may lead to an explanation for part the observed differences between 12 GMT and 0 GMT spectra. The reason for this diurnal difference has been suggested to be associated with daytime heating of the island surface.

Once the annual cycle was removed from the time series, significant peaks with higher frequencies were observed in the recalculated spectra. Most interesting among these were the peaks corresponding to the intraseasonal oscillation (ISO) range of frequencies (periods from 30–60 days). The ageostrophic parameter

was found to have significant peaks at frequencies corresponding to published values for peaks in the power spectra of atmospheric angular momentum (Gutzler and Madden, 1993), OLR anomalies (Lau and Chan, 1985), tropospheric winds (Madden and Julian, 1971 and Madden and Julian, 1972), and GCM simulations of the ISO (e.g. Goswami and Shukla, 1984). The nighttime (12 GMT) spectrum of boundary layer top deviations showed one weak peak in the ISO range as well.

Spectral analysis of nighttime OLR data centered on a grid point near Wake island shows that the strong annual cycle peak and its harmonics dominate the power spectrum. In addition to the peaks associated with the strong annual cycle, a significant peak was found in the ISO range with maximum power at a period of 38 days. Removal of an estimated annual cycle was successful for the nighttime OLR data, but the deviations spectrum yielded no new significant (90% confidence or better) peaks in the ISO range. In the nighttime OLR deviations spectrum the 38 day peak power intensified.

Spectral analysis was also applied to the first three EOF modes of specific humidity profiles from Liu et al., (1991). In each case the spectra were dominated by the annual cycle and its harmonics. With the annual cycle removed, the recalculated spectra showed no common periodicities with the boundary layer top spectra and only a few common periodicities with the ageostrophic parameter spectra. The EOF modes of specific humidity deviations spectra show a few ISO range peaks, all of which are also present in the ageostrophic parameter deviations spectra.

The deviations of the first mode of specific humidity spectrum shows a strong similarity to the spectrum of nighttime OLR data in the ISO range including a common peak at a period of 38 days and may indicate that the first mode represents the influence of convection on specific humidity profiles. The link between the ISO ranges of the ageostrophic parameter spectrum, the nighttime OLR spectrum, and the first mode spectrum seems to indicate that the ageostrophic parameter is related to both the dynamical and thermodynamical aspects of the ISO. Recent work indicates that the ISO is the result of the interaction between dynamics and moist processes (e.g. Cho et al., 1994 and Madden and Julian, 1994).

The ageostrophic parameter exhibits a seasonal shift in period of the major peak in the ISO range similar to the shift described in Hartmann et al., (1992). The period of the major ISO peak in the ageostrophic parameter power spectrum is centered around 50 days in May and is closer to 40 days in December.

Observational evidence in the form of spectral peaks with power maxima near 26 days period in the ageostrophic parameter power spectrum supports the presence of 20–30 day periods in tropical data. Lau and Chang, (1992) reported a 20–30 day period in the velocity potential field. Further study should be undertaken to determine the veracity of the ageostrophic parameter spectral peak and its causes.

The ageostrophic parameter spectra show peaks in the ISO range that correspond to published values for periods of atmospheric angular momentum and outgoing longwave radiation which are both considered tracers for the ISO phenomena. The ageostrophic parameter spectrum also has peaks in the ISO range

similar to the peaks found in the ISO range of spectra of nighttime OLR data. Furthermore, the ageostrophic parameter shares a common peak with the nighttime deviations of boundary layer height spectrum in the ISO range. The ageostrophic parameter is apparently related to the ISO phenomena and is related in such a way as to include aspects of dynamical influences, boundary layer properties, and properties associated with moisture. Study of the ageostrophic parameter's relationship to the ISO should be continued and expanded to include spatial analysis, as well as coherence calculations which can establish that the common frequencies presented here are not just coincidental.

References

Anderson, J.R., D.E. Stevens, and P.R. Julian, 1984: Temporal Variations of the Tropical 40–50 Day Oscillation. *Monthly Weather Review*, **112**, 2431–2438.

Bath, M., 1974: Developments in Solid Earth Geophysics: 7 Spectral Analysis in Geophysics. Elsevier Scientific Publishing Co., Amsterdam. Ch. 3.

Cho, H.R., K. Fraedrich, and J.T. Wong, 1994: Cloud Clusters, Kelvin Wave-CISK, and the Madden-Julian Oscillations in the Equatorial Troposphere. *J. of Atmospheric Sciences*, **51**, 68–76.

Ek, M. and L. Mahrt, 1991: OSU 1–D PBL Model version 1.0.4

Ghil, M. and K. Mo, 1991: Intraseasonal Oscillations in the Global Atmosphere. Part I: Northern Hemisphere and Tropics. *J. of Atmospheric Sciences*, **48**, 752–779.

Gill, A.E., 1980: Some Simple Solutions for Heat-Induced Tropical Circulation. *Quart. J. of Roy. Meteor. Soc.*, **106**, 447–463.

Goswami, B.N. and J. Shukla, 1983: Quasi-Periodic Oscillations in a Symmetric General Circulation Model. *J. of Atmospheric Sciences*, **41**, 20–37.

Gutzler, D.S. and R.A. Madden, 1993: Seasonal Variations of the 40–50–Day Oscillations in Atmospheric Angular Momentum. *J. of Atmospheric Sciences*, **50**, 850–860.

Hartmann, D.L. and J.R. Gross, 1988: Seasonal Variability of the 40–50 Day Oscillation in Wind and Rainfall in the Tropics. *J. of Atmospheric Sciences*, **45**, 2680–2702.

Hartmann, D.L., M.L. Michelsen, and S.A. Klein, 1992: Seasonal Variations of Tropical Intraseasonal Oscillations: A 20–25–Day Oscillation in the Western Pacific. *J. of Atmospheric Sciences*, **49**, 1277–1289.

Hastenrath, S., 1990: Climate Dynamics of the Tropics. Kluwer Academic Publishers, Dordrecht. Ch. 6.

Hayashi, Y. and D.G. Golder, 1986: Tropical Intraseasonal Oscillations Appearing in a GFDL General Circulation Model and FGGE Data. Part I: Phase Propagation. *J. of Atmospheric Sciences*, **43**, 3058–3067.

Holton, J.R., 1992: An Introduction to Dynamic Meteorology, 3rd Edition. Academic Press, New York.

Knutson, T.R. and K.M. Weickmann, 1986: 30–60 Day Atmospheric Oscillations: Composite Life Cycles of Convection and Circulation Anomalies. *Monthly Weather Review*, **115**, 1407–1436.

Lau, K. and P.H. Chan, 1985: Aspects of the 40–50 Day Oscillation During the Northern Winter as Inferred from Outgoing Longwave Radiation. *Monthly Weather Review*, **113**, 1889–1909.

Lau, K.M. and L. Peng, 1987: Origin of Low-Frequency (Intraseasonal) Oscillations in the Tropical Atmosphere Part I: Basic Theory. *J. of Atmospheric Sciences*,**44**, 950–972.

Levy, G. and C.S. Bretherton, 1987: On a Theory of the Evolution of Surface Cold Fronts. *J. of Atmospheric Sciences*, **44**, 3413–3418.

Liu, W.T., W. Tang, and P.P. Niiler, 1991: Humidity Profiles Over the Ocean. *J. of Climate*, **4**, 1023–1034.

Madden, R.A., 1986: Seasonal Variations of the 40–50 Day Oscillation in the Tropics. *J. of Atmospheric Sciences*, **43**, 3138–3158.

Madden, R.A., 1988: Large Intraseasonal Variations in Wind Stress Over the Tropical Pacific. *J. of Geophysical Research*, **93**, 5333–5340.

Madden, R.A. and P.R. Julian, 1971: Detection of a 40–50 Day Oscillation in the Zonal Wind in the Tropical Pacific. *J. of Atmospheric Sciences*, **28**, 702–708.

Madden, R.A. and P.R. Julian, 1972: Description of Global-Scale Circulation Cells in the Tropics with a 40–50 Day Period. *J. of Atmospheric Sciences*, **29**, 1109–1123.

Madden, R.A. and P.R. Julian, 1994: Observations of the 40–50–Day Tropical Oscillation — A Review. *Monthly Weather Review*, **122**, 814–837.

Mahrt, L. and J. Howell, 1994: The Influence of Coherent Structures and Microfronts on Scaling Laws Using Global and Local Transforms. *J. of Fluid Mech.*, **260**, 247–270.

Mysak, L.A. and G.J. Mertz, 1984: A 40–60 Day Oscillation in the Source Region of the Somali Current During 1976. *J. of Geophysical Research*, **89**, 711–715.

Press, W.H., S.A. Teukolsky, W.T. Vetterling, and B.P. Flannery, 1992: Numerical Recipes in FORTRAN The Art of Scientific Computing Second Edition. Cambridge University Press, New York.

Scargle, J.D., 1982: Studies in Astronomical Time Series Analysis II. Statistical Aspects of Spectral Analysis of Unevenly Spaced Data *Astrophysical Journal*, **263**, 835–853.

Stull, R.B., 1988: An Introduction to Boundary Layer Meteorology. Kluwer Academic Publishers, Dordrecht.

Terada, K. and M. Hanzawa, 1984 : Climate of the North Pacific Ocean. World Survey of Climatology Volume 15: Climate of Oceans. Elsevier Science Publishers, Amsterdam. Kluwer Academic Publishers, Dordrecht. Edited by H. Van Loon, 432–491.

Wallace, J.M., 1971: Spectral Studies of Tropospheric Wave Disturbances in the Tropical Western Pacific. *Rev. Geophysics*, **9**, 557–612.

Wallace, J.M., 1972: Empirical Orthogonal Representation of Time Series in the Frequency Domain. Part I: Theoretical Considerations *J. of Applied Meteorology*, **11**, 887–892.

Wallace, J.M. and C.P. Chang, 1969: Spectrum Analysis of Large-Scale Atmospheric Waves in the Tropical Lower Troposphere. *J. of Atmospheric Sciences*, **26**, 1010–1025.

APPENDIX

Appendix A: Testing of Modified Periodogram

Using the modified periodogram algorithm spectra of known functions were computed to verify the ability of the routine. The functions were sampled with the same spacing as the worst case instance of the paper. The first test as shown in figure 33 is the spectra calculated on data derived from the function $y=\sin(\pi/4t)$. The peak shown in the figure is located at a frequency of 0.125 which is equivalent to $\pi/4$ radians.

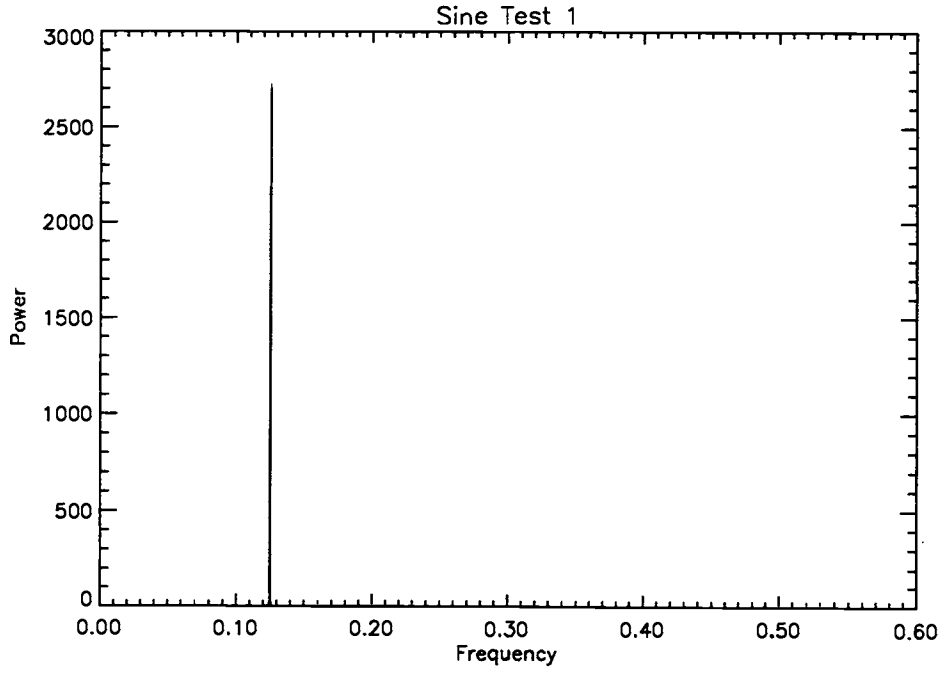

Figure 33 Sine Test One

The second test uses a spectrum calculated from the function $y=\sin(\pi/4t)+\sin(3\pi/4t)$ and is shown in figure 34. The spectrum shows two

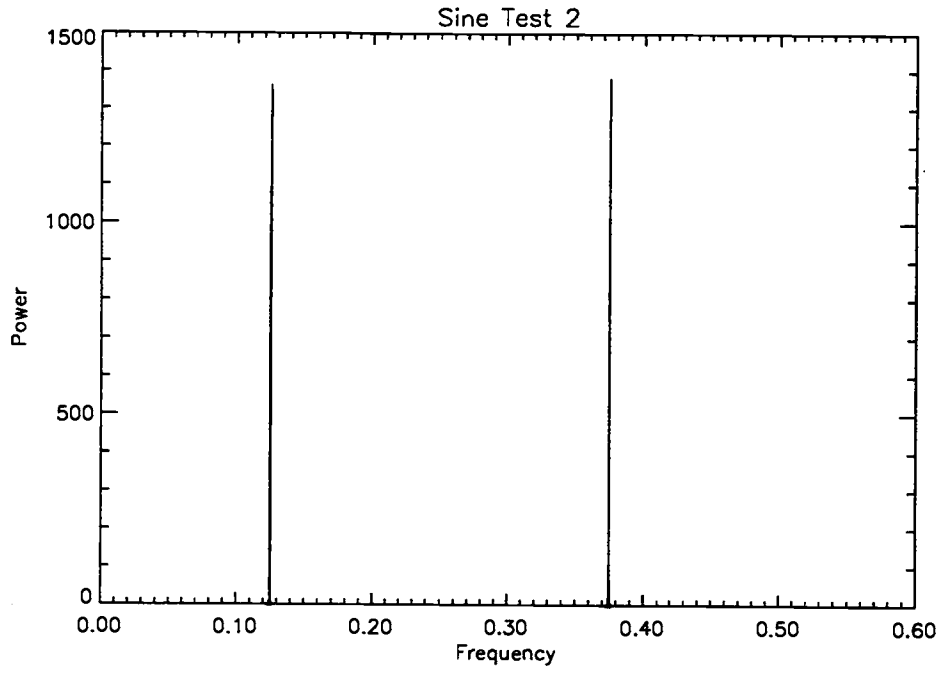

Figure 34 Sine Test Two

peaks one corresponding to a frequency of 0.125 and another at a frequency of 0.375 which is $3\pi/4$ radians.

Figure 35 shows the spectrum for test three which was computed with the function $y=10\sin(\pi/4t)+\sin(3\pi/4t)$. The spectrum again shows two peaks

corresponding to $\pi/4$ and $3\pi/4$, but the $\pi/4$ peak is now substantially larger than the now reduced $3\pi/4$ peak.

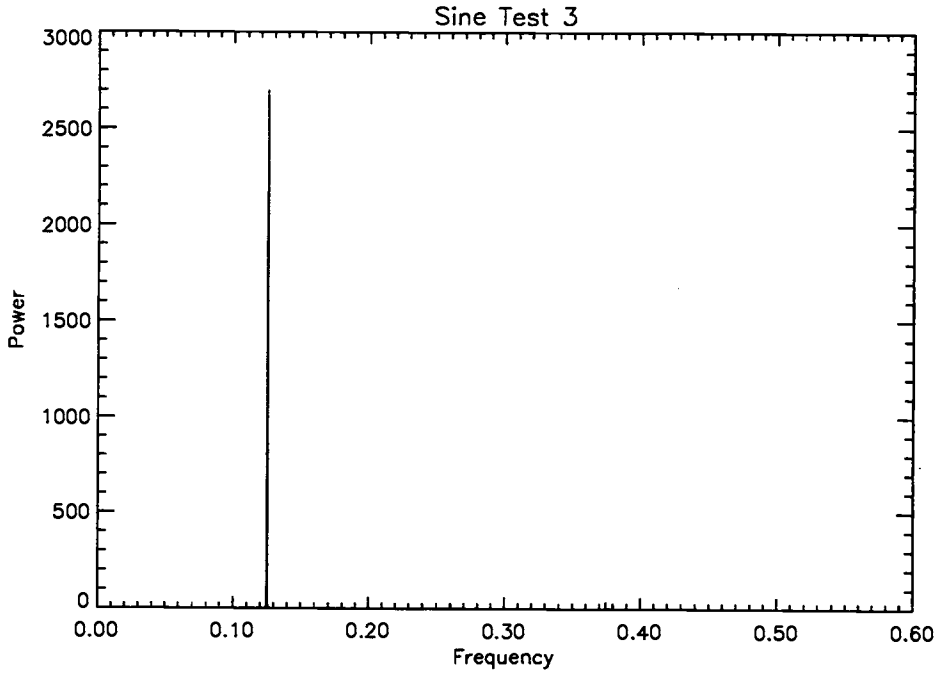

Figure 35 Sine Test Three